

Generative Transformer for Accurate and Reliable Salient Object Detection

Yuxin Mao, Jing Zhang, Zhexiong Wan, Yuchao Dai*,
Aixuan Li, Yunqiu Lv, Xinyu Tian, Deng-Ping Fan and Nick Barnes

Abstract—Transformer networks, which originate from machine translation, are particularly good at modeling long-range dependencies within a long sequence. Currently, transformer networks are making revolutionary progress in various vision tasks ranging from high-level classification tasks to low-level dense prediction tasks, leading to significant performance improvements compared with convolutional neural network (CNN) based frameworks. In this paper, we conduct extensive research on exploring the contribution of transformers to salient object detection, achieving both accurate and reliable saliency predictions. We first investigate transformers for accurate salient object detection with deterministic neural networks, and explain that the effective structure modeling and global context modeling abilities lead to its superior performance compared with the CNN based frameworks. Then, we design stochastic networks to evaluate the transformers' ability in reliable salient object detection. We observe that both CNN and transformer based frameworks suffer greatly from the over-confidence issue, where the models tend to generate wrong predictions with high confidence, leading to over-confident predictions or a poorly-calibrated model. To estimate the calibration degree of both CNN- and transformer-based frameworks for reliable saliency prediction, we introduce generative adversarial network (GAN) based models to identify the over-confident regions by sampling from the latent space. Specifically, we present the inferential generative adversarial network (iGAN). Different from the conventional GAN based framework, which defines the distribution of the latent variable as fixed standard normal distribution $\mathcal{N}(0, \mathbf{I})$, the proposed "iGAN" infers the latent variable by gradient-based Markov Chain Monte Carlo (MCMC), namely Langevin dynamics. We apply the proposed inferential generative adversarial network (iGAN) to both fully and weakly supervised salient object detection, and explain that iGAN within the transformer framework leads to both accurate and reliable salient object detection. The source code and experimental results are publicly available via our project page: <https://github.com/fupiao1998/TrasformerSOD>.

Index Terms—Vision Transformer, Salient Object Detection, Inferential Generative Adversarial Network.

1 INTRODUCTION

Visual salient object detection (SOD) [1]–[7] aims to localize the regions of an image that attract human attention, which is usually defined as a binary segmentation task. For static image based SOD, researchers mostly consider one of the two fully supervised tasks, namely RGB image based SOD [1], [2] and RGB-D image pair based SOD [3], [4]. To reduce the labeling effort, several weakly supervised SOD models have been proposed to learn saliency with image-level supervision [6], scribble supervision [5] or learn saliency directly from noisy labeling [8], [9].

Before the deep learning revolution, conventional SOD models [10], [11] used handcrafted features as shown in Fig. 2, which generally define saliency as contrast [12] between each pixel (or superpixel) and the other pixels (or superpixels). In this way, the receptive field of the conventional handcrafted-feature based models is the entire image, which is the global context. However, the less representative of those handcrafted features limited the performance of the conventional methods, especially for complex scenarios. Deep convolutional neural network (CNN) based SOD models [1], [2], [13], [14] achieve significant performance improvement compared with handcrafted feature based techniques

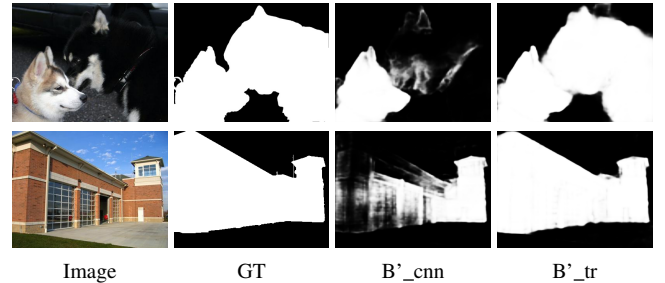


Fig. 1. Saliency predictions of a CNN based model (B'_{cnn}) and a transformer based model (B'_{tr}) for images with large salient objects.

since more sophisticated features are extracted from the deep network.

Deep SOD frameworks usually contain two main parts: an encoder to extract different levels of features, and a decoder to aggregate features from different levels of the network for final prediction. The encoder part is usually adopted from an ImageNet pre-trained backbone network, *e.g.*, VGG [18], ResNet [19]. In this way, SOD models are mainly designed to obtain effective decoders for feature aggregation [1], [2], [20]. Conventional CNN backbones have gradually larger receptive fields with the deeper layers. But the larger receptive field is obtained with a loss of structure information as a sacrifice, this is the main issue of these backbone networks for SOD. This is the reason for incorporating the additional complicated decoders. Note that, once the information is lost, it will not be fully recovered. Further, although the

- Yuxin Mao, Zhexiong Wan, Yuchao Dai, Aixuan Li, Yunqiu Lv and Xinyu Tian are with School of Electronics and Information, Northwestern Polytechnical University, China.
- Jing Zhang and Nick Barnes are with School of Computing, Australian National University.
- Deng-Ping Fan is with the CS, Nankai University, Tianjin, China.
- Corresponding author: Yuchao Dai (Email: daiyuchao@nwpu.edu.cn).

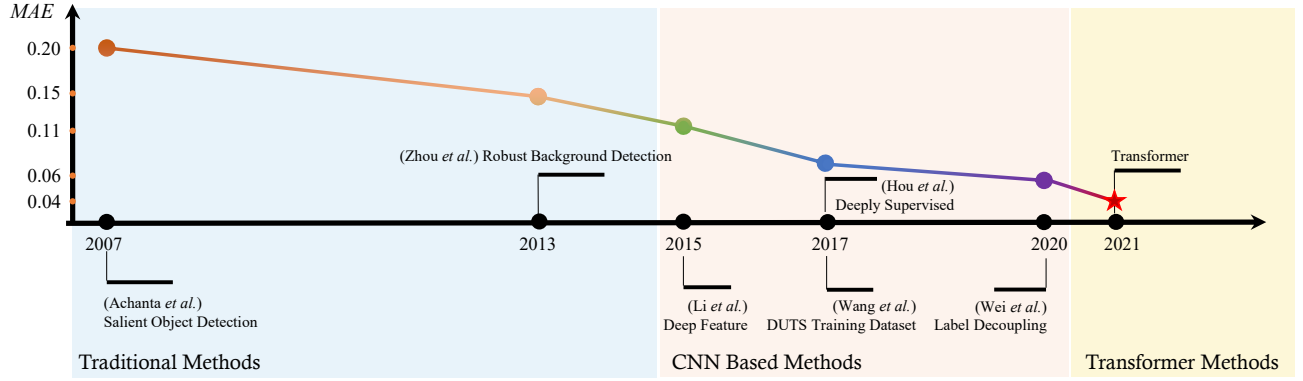


Fig. 2. A simplified timeline of SOD models, where the y-axis shows the mean absolute error (MAE) of related models on the DUT testing dataset [11]. Initially, Itti *et al.* [15] defined saliency detection as fixation prediction to predict the fixation points of salient objects. Then, Achanta *et al.* [16] introduced saliency detection as binary segmentation task to produce a segmentation map instead of a fixation map. The first CNN based deep saliency model [17] appeared in 2015, which replaced the handcrafted features with deep features. We investigate transformer based SOD models with significantly improved model performance.

theoretical receptive field of a CNN covers the entire image [21], many studies have shown that the actual receptive field of a CNN is much smaller, making it less effective in localizing the large objects (see “B’_cnn” in Fig. 1). In this way, a network with a larger receptive field without losing fine-grained information can be beneficial for context based tasks, *e.g.*, SOD, to achieve effective context modeling.

Researchers have found that the “Transformer” [22] has great potential to solve the limited receptive field issue in vision tasks. The advantage of the “Transformer” lies in the use of self-attention to capture global contextual information to establish a long-range dependency. Different from convolutional neural networks that focus on a small patch of the image with a sliding-window-wise convolution operation, the transformer network [22] performs global context modeling with self-attention. Inspired by [23], [24] and the accurate structure modeling ability of transformer, we conduct extensive research to explore the contribution of the transformer for accurate and reliable SOD.

Firstly, we investigate transformer networks for accurate SOD with deterministic neural networks, and explain that the effective structure modeling and global context modeling abilities lead to its superior performance compared with the CNN based frameworks. Secondly, we aim to analyse the calibration degree [25] of the transformer-based framework for reliable saliency prediction. Specifically, we present an inferential generative adversarial network (iGAN). Different from the conventional generative adversarial network (GAN) [26] which defines the distribution of the latent variable as fixed standard normal distribution $\mathcal{N}(0, \mathbf{I})$, the proposed “iGAN” infers the latent variable by gradient based Markov chain Monte Carlo (MCMC), namely Langevin dynamics [27]. Lastly, we apply the proposed iGAN to both fully and weakly supervised SOD, and explain that iGAN within the transformer framework leads to both accurate and reliable SOD, where the produced uncertainty map [28] can effectively explain model prediction, leading to well-calibrated model.

Our main contributions are: 1) we extensively explore the contribution of transformer networks [22]–[24], [29] for accurate SOD and explain that the effective structure and global context modeling abilities lead to the superior performance of the transformer-based saliency detection network; 2) we introduce an inferential generative adversarial network (iGAN) to effectively

measure the calibration degree of the transformer-based SOD network, leading to reliable saliency prediction; 3) we apply iGAN to fully and weakly supervised SOD to extensively explore the proposed new generative model within the transformer framework.

2 RELATED WORK

Salient Object Detection: SOD aims to detect and segment the objects that attract human attention, which is driven by visual attention [15]. In this way, salient objects are defined as objects that have strong contrast, and early work usually utilized this prior for saliency related feature extraction. Currently, the mainstream of saliency detection models are deep convolutional neural network based, which usually take the trained backbone network [18], [19] as encoder, and most of the effort is then to design effective decoders to achieve high-low level feature aggregation [1], [2], [13], [14], [20], [30]. Wu *et al.* [1] propose a “stacked cross refinement network”, and use the interaction between the edge module and the detection module to optimize the two tasks at the same time. Wei *et al.* [2] introduce an adaptive selection of complementary information when aggregating multi-scale features with a structure-aware loss function. Qin *et al.* [31] use deep supervision for the encoder-decoder network and design an extra residual refinement module with high-quality boundary supervision to obtain a more refined saliency map. [32] integrates the information of adjacent layers, and integrates multi-scale information to retain the internal consistency of each category (salient foreground or non-salient background). Tang *et al.* [33] model the two tasks of discriminating salient regions and identifying accurate edges independently, and solved the limitations of low-resolution SOD by using low-resolution images to delineate salient regions and using high-resolution to refine salient regions. Unlike the mainstream design refinement prediction networks, Zhang *et al.* [34] propose an automatic consolidation of multi-level features based on neural architecture search for flexible integration of information at different scales.

With extra depth information, RGB-D image pair based SOD models [3], [4], [35], [36] mainly focus on exploring the complementary information between the RGB image and the depth data for effective multi-modal learning. Depending on how information from these two modalities is fused, existing RGB-D SOD models can be divided into three categories: early-fusion models [3],

[37], late-fusion models [38]–[40] and cross-level fusion models [4], [36], [41]–[52]. The early-fusion models fuse RGB image and depth data at the input layer, forming a four-channel feature map. The late fusion models treat each mode (RGB and depth) separately, and then saliency fusion is achieved at the output layer. The cross-level fusion models gradually fuse feature of RGB and depth [4], [45], [46], [48], [50]–[57], which is the main stream for RGB-D SOD.

Vision Transformer and Its Applications: The transformer network [22], which uses multi-head self-attention modules with positional encoding to capture long-range dependencies between every two elements in an input sequence, has achieved great success in natural language processing (NLP). This breakthroughs has sparked great interest in the computer vision community to adapt these models for vision tasks such as object detection [58]–[62], object tracking [63]–[65], pose estimation [66], [67], optical flow [68] *etc.* Inspired by the success of the Vision Transformer (ViT) [29] in the task of image classification which splits the input image into a sequences of patches and feeds them to a standard Transformer encoder, some works extend transformer for dense prediction tasks, *e.g.*, semantic segmentation or depth estimation. SETR [69] and PVT [61] use several convolutional layers as the decoder to upsample feature maps and get the dense prediction with the input image size. DPT [23] uses ViT [29] as encoder to extract features from different spatial resolutions of the initial embedding. Then a decoder assembles the set of tokens into grid representations at each resolutions. Liu *et al.* [24] present the Swin Transformer, a hierarchical transformer with a shifted windowing scheme to achieve an efficient network for vision tasks.

Recently, [70], [71] introduce the transformer to saliency detection, achieving significant performance improvement compared with the CNN based saliency models. Different from [70], which works on accurate saliency detection with a deterministic network, we present a generative model based framework for both accurate and reliable saliency detection. Different from [71], which adopts energy-based model [72] for modeling the prior distribution of the latent variable, we present an alternative solution by modeling the prior distribution of a generative adversarial network with Langevin Dynamics [27], leading to image conditioned prior distribution, named inferential GAN (iGAN). We also apply the proposed iGAN to weakly supervised SOD and explain the superior performance of iGAN within the transformer based framework, which has never been explored before.

Generative Models and Their Applications: There mainly exist two types of generative models, namely latent variable models [26], [73] and energy-based models [72]. The former usually involve an extra latent variable to model the predictive distribution, and the latter directly estimate the compatibility of the input and output variable with a designed energy function. The variational auto-encoder (VAE) [73], [74] and generative adversarial network (GAN) [26] are two widely studied latent variable models. VAEs use extra inference model to constrain the distribution of the latent variable, and GANs design a discriminator to distinguish real samples and the generated samples. VAEs have already been successfully applied to image segmentation [75], [76] to produce stochastic predictions during testing. For saliency prediction, [77] adopts a VAE for image background reconstruction, and the residual of the raw image and the reconstructed background is then defined as the salient region(s). Differently, [3], [78] design conditional variational auto-encoder (CVAE) to model the subjective nature of saliency, where the latent variable is used to

model the prediction variants. GAN-based methods can be divided into two categories, namely fully-supervised and semi-supervised settings. The former [79], [80] uses the discriminator to distinguish model predictions from ground truth, while the latter [81], [82] rely on the GAN to explore the contribution of unlabeled data. [83] introduce a inferential Wasserstein GAN (iWGAN) model, which is a principled framework to fuse auto-encoders and WGANs and jointly learns an encoder network and a generator network motivated by the iterative primal dual optimization process.

Weakly Supervised Segmentation Models: Instead of label-consuming pixel-wise annotations, Weakly Supervised Segmentation (WSS) models are designed to explore the possibility of using weak labels, *e.g.*, image tags [84]–[88], bounding box [89]–[93], scribble [5], [94]–[96], point [97]–[99], as supervision. The typical method [90], [94], [100] usually considers the initial segmentation map produced by traditional unsupervised methods, such as MCG [101] and GrabCut [102], as the supervision to train the deep neural network and then repeat the iterative process between the refinement of the prediction and the training of the network. However, the framework tends to introduce accumulated label noise in each step and the iteration is time-consuming. Zhang *et al.* [8] propose an end-to-end deep learning framework to predict the latent saliency map from multiple noisy saliency maps created by unsupervised handcrafted saliency methods and mitigate the influence of label noise by a specifically-designed noise modeling module. The idea is further extended [103] to use a generative model [104] to model the label noise from a single noisy saliency map. In addition to noise modeling strategies, some methods refine the segmentation map with structure-aware loss functions. Yu *et al.* [96] use partial cross entropy loss to expand the scribble region to the whole object region and refine the segmentation with a local saliency coherence loss. Tian *et al.* [93] directly refine the object from coarse label by a deep neural network using the projection loss based on tightness prior of bounding box and pairwise affinity loss to assign proximal pixels to the same category. Currently, most WSS methods are based on CNNs. In this paper, we explore the potential of transformers for weakly supervised segmentation, especially weakly supervised SOD with scribble supervision [5], [96].

3 TRANSFORMER NETWORK: AN OVERVIEW

Here we introduce the transformer network, especially the vision transformer structure. We first introduce the core modules, Multi-Head Self Attention (MSA) module.

Multi-Head Self Attention: The self-attention mechanism aims to estimate the relevance of two items, which explicitly models the interactions between all items of a sequence. We denote a sequence $X \in \mathbb{R}^{n \times d}$, where n is the sequence length and d is the embedding dimension as input vector. The input vector is first transformed into three different vectors: the query vector Q , the key vector K and the value vector V with the same dimension d . This is done by defining three learnable weight matrices $W^Q \in \mathbb{R}^{n \times d_q}$, $W^K \in \mathbb{R}^{n \times d_k}$ and $W^V \in \mathbb{R}^{n \times d_v}$. The input sequence X is projected onto these weights to get:

$$Q = XW^Q, K = XW^K, V = XW^V. \quad (1)$$

Based on the above three weights, we compute the dot-product of the query with all keys, and normalize into attention scores using the softmax operator. Finally, each value vector is multiplied by the sum of the attention scores. In this way, vectors with larger

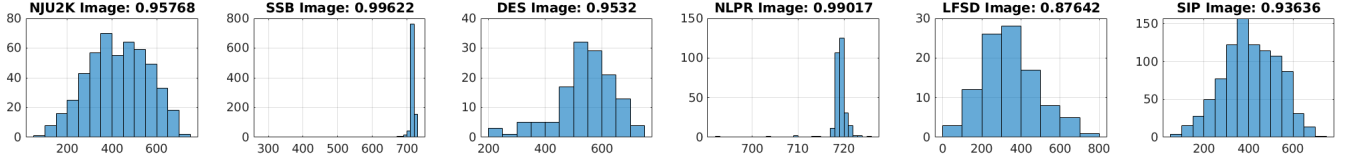


Fig. 3. Global contrast of depth from benchmark RGB-D SOD dataset, where the x-axis is the Chi-squared distance between salient foreground and non-salient background within the depth data, and y-axis is the number of images.

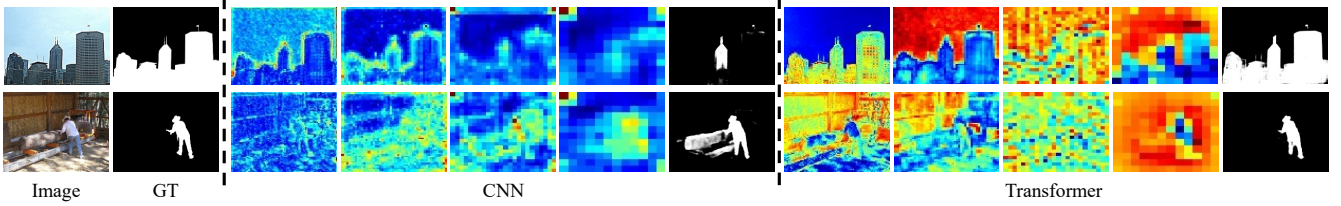


Fig. 4. Different levels of backbone features of the ResNet50 backbone [19] ("CNN") and the transformer backbone ("Transformer") after fine-tuning them for salient object detection.

attention scores receive additional focus from the following layers. The definition of scaled dot-product self-attention is:

$$Z = \text{softmax}\left(\frac{QK^T}{\sqrt{d}}\right)V. \quad (2)$$

To solve the issue that the input vectors lack location information, an additional positional encoding is added to the inputs. The self-attention is then extended to multi-head self-attention to project the inputs into different representations by different heads with different weights. The outputs are concatenated to pass into the feed forward multilayer perceptron.

Transformer: The vanilla Transformer [22] is composed of multi-layer encoder/decoder modules, and was firstly applied to the machine translation task in neural language processing. Each encoder is composed of a multi-head self attention layer and a feed-forward network, while each decoder is composed of a multi-head self attention layer, an encoder-decoder attention layer and a feed-forward network [105].

Vision Transformer: The vision transformer can be used for dense prediction tasks, *e.g.*, semantic segmentation or depth estimation [23], [24]. For a typical vision transformer, the input image $x \in \mathbb{R}^{H \times W \times C}$ is split into a sequence of patches (or tokens) $x = [x_1, \dots, x_N] \in \mathbb{R}^{N \times P^2 \times C}$ with patch size (P, P) , where C is channel size of image x . Then each token is linearly projected to a sequence of one dimensional patch embedding feature vectors as $e_x = [E x_1, \dots, E x_N] \in \mathbb{R}^{N \times d}$, where E is the embedding function, and d is the dimension of the feature. The learnable position embeddings are then added to the tokens as $z = e_x + \text{pos}$ in order to preserve the spatial location information, where pos represents the learnable position embeddings.

With the tokenization of input image x , all the tokens z are fed into a transformer encoder with L transformer layers. Each transformer layer includes a MSA module and a feed forward multilayer perceptron (MLP) block with residual connections and layer normalization. The l -th, $l \in \{1, \dots, L\}$ transformer layer can be expressed as:

$$\begin{aligned} a^{l-1} &= \text{MSA}(\text{LN}(z^{l-1})) + z^{l-1}; \\ z^l &= \text{MLP}(\text{LN}(a^{l-1})) + a^{l-1}. \end{aligned} \quad (3)$$

The state at the output of the transformer encoder (z^L) then serves as the image representation.

In order to further improve the computational efficiency of the vision transformer structure, Swin transformer [24] proposes window-based self-attention and shifts the window to introduce connections between neighboring non-overlapping windows. So each Swin transformer block is computed as:

$$\begin{aligned} \hat{z}^l &= \text{W-MSA}(\text{LN}(z^{l-1})) + z^{l-1}; \\ z^l &= \text{MLP}(\text{LN}(\hat{z}^l)) + \hat{z}^l; \\ \hat{z}^{l+1} &= \text{SW-MSA}(\text{LN}(z^l)) + z^l; \\ z^{l+1} &= \text{MLP}(\text{LN}(\hat{z}^{l+1})) + \hat{z}^{l+1}, \end{aligned} \quad (4)$$

where W-MSA and SW-MSA are window based multi-head self-attention using regular and shifted window, respectively.

4 ACCURATE AND RELIABLE SALIENT OBJECT DETECTION VIA TRANSFORMER

4.1 Task Analysis

There are two types of settings for static image based saliency detection, namely RGB image saliency detection and RGB-D image pair saliency detection. The former involves two variables, namely the RGB image x and its corresponding ground truth saliency map y . The conventional practice of RGB image-based saliency detection involves training a model to achieve a mapping from the input space (RGB image) to the output space (saliency map), which is usually defined as a single modal problem. The main focus of existing RGB image based saliency detection models [1], [2] is achieving structure-accurate prediction with effective high/low level feature aggregation or structure-aware loss functions. RGB-D image pair-based saliency detection involves three main variables, including the input image x , depth d and ground truth saliency map y . The model is then trained to map x and d to the saliency map y . With extra geometric information from the depth data, RGB-D saliency detection is usually defined as a multi-modal learning problem, and the main focus of existing models [4], [35], [36], [52] is to design multi-modal learning frameworks for effective RGB feature and depth feature fusion. By thoroughly analysing the saliency detection models, we observe

three main issues within existing techniques, namely less effective global context modeling, missing structure information and the inconsistent depth distribution issue.

Less effective global context modeling: The conventional CNN-based saliency detection models rely on a convolution operation with stride or pooling to obtain a larger receptive field. We claim that the sliding window based convolution operation limits its context modeling ability, especially the global context modeling ability, which is important for detecting large salient object (see Fig. 1). We have thoroughly analysed the failure cases of existing state-of-the-art saliency detection models, and observed that the less effective global context modeling caused by limited receptive fields is one of the main issue that hinder the performance of deep saliency detection models.

Missing structure information: The usage of the stride operation or pooling within the existing CNN backbone-based framework leads to extensive down-sampling of the backbone features as shown in Fig. 4 (“CNN”), where we show the different levels of backbone features of the ResNet50 [19] after fine-tuning it for SOD. We observe missing structure information in both higher level features and lower level features, which makes effective high/low level feature aggregation and structure-aware loss function necessary for CNN backbone based framework to recovery the missing structure information.

Inconsistent depth contrast distribution: For RGB-D saliency detection, extra depth data is involved. We claim that depth from different sensors has different contrast distributions, leading to inconsistent input distributions across the training and testing datasets. We compute the global contrast of the depth data from different testing datasets and show the global depth contrast in Fig. 3. The global contrast measures the noticeability of the salient object. To obtain the global contrast of the depth data, we first compute a $3H$ dimensional color histogram of both the salient foreground and background of the depth data. Following [106], we obtain an $H = 16$ dimensional histogram for the Red, Green and Blue channel¹ of the RGB image respectively, and the histogram of the color image is then the concatenation of the above histograms. Then we adopt the Chi-squared distance to measure the global contrast between the salient object and background. We define the mean of the Chi-squared distance as the global depth contrast. Fig. 3 clearly shows that the global contrast of the salient foreground with the depth data varies across the testing dataset. Similarly, we obtain the RGB image global contrast, and compute the global contrast difference of the RGB image and depth for each testing dataset, which is shown in the title of each figure in Fig. 3. The various global contrast differences of RGB image and depth data further explain the different contribution of depth.

4.2 Necessity of Accurate and Reliable Model

Accurate Saliency Model: As a context-based task, SOD relies on both local and global context. Conventional CNN backbone-based frameworks [1], [20] are effective in modeling the local context, while the limited receptive field makes them less effective in modeling the global context (see Fig. 1), leading to less accurate prediction for larger salient objects. The self-attention model within the transformer framework enables it to achieve long-range dependency modeling, thus it can obtain effective global context modeling, which in turn is beneficial for accurate SOD.

1. For gray image, we obtain its color version by concatenating it channel-wise to obtain the three channel color image.

Reliable Saliency Model: The reliability of a model tells us the degree to which we can trust the model’s prediction. This can be assessed by comparing the model prediction against the actual ground truth. Existing point-to-point estimation frameworks are built upon the deterministic learning pipeline, where the model is trained to achieve mapping from the input space to the output space. However, the deterministic mapping fails to explain how model is confident on its prediction. As deep neural network can fit any random noise [25], the trained model can be biased, caused by the randomness of the data, *e.g.*, inherent labeling noise, accuracy of the data acquisition sensors, or biased distribution of the training dataset, *e.g.* unbalanced or less diverse data. In this way, over-confident models pose a serious issue for the reliability of the model. Further, for real-life applications, the “actual ground truth” for new samples are usually unavailable, making the “deterministic mapping” based framework less effective in modeling the reliability of the model.

For SOD, there are two types of biases: labeling noise and subjective nature [78]. For the former, the inevitable labeling noise exists while labeling the pixel-wise ground truth. For the latter, due to different preferences, the provided saliency ground truth can only reflect the majority saliency opinion of labellers for the input image, which is not comprehensive in explaining the “subjective nature” of saliency. The two types of biases introduce “uncertainty” to the model, where [28] defines uncertainty caused by the former as “aleatoric uncertainty”, and the latter as “epistemic uncertainty”. A reliable saliency model should produce accurate prediction with auxiliary reliability degree estimation, making it possible to explain model prediction.

4.3 Transformer for Accurate Saliency Detection

4.3.1 Network Details

The straightforward solution of using a transformer is to replace the CNN backbone with a transformer backbone, leading to the “transformer encoder”. We take the Swin transformer [24] as our transformer encoder, which takes the embedded image features as input and produces a list of feature maps $f_{\theta_1}(x) = \{t_l\}_{l=1}^4$ of channel size 128, 256, 512 and 1024 respectively, representing different levels of features. Different from [23], [29] that use fixed tokenization, the Swin transformer [24] is a hierarchical transformer structure whose representation is computed with self-attention in shifted non-overlapped windows, thus it enables even larger receptive field modeling.

Given the “transformer encoder” $f_{\theta_1}(x) = \{t_l\}_{l=1}^4$, to obtain pixel-wise prediction, we design a simple “convolution decoder” to achieve high/low level feature aggregation. Specifically, we first feed each backbone feature t_l to a simple convolutional block, and obtain the new backbone feature $\{s_l\}_{l=1}^4$ of same channel size $C = 32$. Such channel reduction operation aims to further enhance context modeling and reduce the huge memory requirement. Our final saliency map is then obtained via:

$$s = msd(rcab(concat(\{conv(t_l)\}_{l=1}^4))), \quad (5)$$

where “concat” is the channel-wise concatenation operation, “rcab” is the residual channel attention block, “conv” is a 3×3 convolutional layer and “msd” is the multi-scale dilated convolutional block to obtain an one-channel saliency map $s = f_{\theta_2}(\{t_l\}_{l=1}^4)$. Note that, $\theta = \{\theta_1, \theta_2\}$ indicates the entire parameters of our saliency object detection network, and θ_1 represents the parameters of the encoder, θ_2 represents the parameters of the

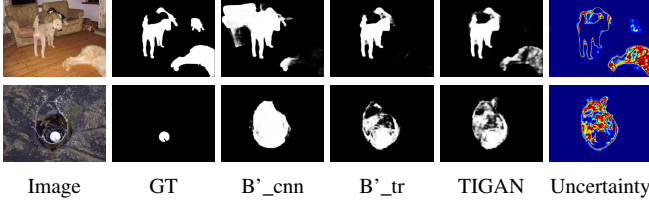


Fig. 5. Predictions of the deterministic CNN (B'_{cnn}) and transformer (B'_{tr}) backbone models, and the proposed iGAN based model (TIGAN) with a transformer backbone. “Uncertainty” is the uncertainty map.

decoder. $f_\theta(x)$ can produce directly the saliency map for RGB image x . For RGB-D saliency detection, we perform early fusion by simply concatenating the RGB image and depth data at input layer, and feed it to a 3×3 convolutional layer to generate new input tensor x' with channel size of 3, which is then feed to the saliency generator θ .

4.3.2 Loss Function

To train the model, the weighted structure-aware loss [2] is adopted, which is the sum of weighted binary cross-entropy loss and weighted IOU loss:

$$\mathcal{L}(s, y) = \omega * \mathcal{L}_{ce}(s, y) + \mathcal{L}_{iou}(s, y), \quad (6)$$

where y is the ground truth saliency map, ω is the edge-aware weight, which is defined as $\omega = 1 + 5 * |(ap(y) - y)|$, with $ap(\cdot)$ representing the average pooling operation. \mathcal{L}_{ce} is the binary cross-entropy loss. \mathcal{L}_{iou} is the weighted IOU loss, which is defined as:

$$\mathcal{L}_{iou} = 1 - \frac{\omega * inter + 1}{\omega * union - \omega * inter + 1}, \quad (7)$$

where $inter = s * y$, and $union = s + y$.

4.3.3 Auxiliary Depth Estimation

As we discussed before, the inconsistent depth contrast distribution may hinder the performance of existing RGB-D saliency detection models. We then propose an auxiliary depth estimation module to solve the “distribution gap” issue within the existing RGB-D saliency detection datasets. The auxiliary depth estimation module has the same structure as our saliency decoder θ_2 , which takes the backbone feature $f_{\theta_1}(x') = \{t_l\}_{l=1}^4$ as input, and outputs a one channel depth map. Within this framework, the final loss function has extra depth related loss:

$$\mathcal{L}_{depth} = \alpha(\beta * \mathcal{L}_{ssim} + (1 - \beta) * \mathcal{L}_1), \quad (8)$$

where $\alpha = 0.1$ is used to control the contribution of the auxiliary depth estimation module, and following the conventional setting, we set $\beta = 0.85$ in this paper. \mathcal{L}_{ssim} is the SSIM loss function [107] and \mathcal{L}_1 is the L1 loss.

4.4 Generative Model for Reliable Saliency Detection

As a deep neural network can fit any random noise [25], the deterministic CNN and transformer backbone based models have serious over-confidence issues, leading to poorly calibrated models. In Fig. 5, we visualize predictions of deterministic CNN and transformer backbone based models, which clearly explain the over-fitting issue of both models, and make wrong predictions

with high confidence. To relieve the over-confidence issue for model reliability estimation, one can use generative models [26], [73], [104] instead of deterministic models to produce stochastic predictions, thus predictive distribution can be estimated. There mainly exists three types of generative model, namely Generative Adversarial Nets (GAN) [26], Variational Auto-encoder (VAE) [73] and Alternating back-propagation [104].

Generative Adversarial Nets: Within the GAN-based framework, we design an extra fully convolutional discriminator g_β following [82], where β is the parameter set of the discriminator. Two different modules (the saliency generator f_θ and the discriminator g_β in our case) play the minimax game in GAN based framework:

$$\min_{f_\theta} \max_{g_\beta} V(g_\beta, f_\theta) = E_{(x,y) \sim p_{data}(x,y)} [\log g_\beta(y|x)] + E_{z \sim p(z)} [\log(1 - g_\beta(f_\theta(x, z)))], \quad (9)$$

where $p_{data}(x, y)$ is the joint distribution of training data, $p(z)$ is the prior distribution of the latent variable z , which is usually defined as $p(z) = \mathcal{N}(0, \mathbf{I})$.

In practice, we define loss function for the generator as the sum of a reconstruction loss \mathcal{L}_{rec} , and an adversarial loss \mathcal{L}_{adv} , which is $\mathcal{L}_{gen} = \mathcal{L}_{rec} + \lambda \mathcal{L}_{adv}$, where the hyper-parameter λ is tuned, and empirically we set $\lambda = 0.1$ for stable training. For saliency detection, we define the reconstruction loss \mathcal{L}_{rec} as the structure-aware loss as in Eq. 6. The discriminator g_β is trained via the loss function: $\mathcal{L}_{dis} = \mathcal{L}_{ce}(g_\beta(f_\theta(x, z)), 0) + \mathcal{L}_{ce}(g_\beta(y), 1)$, where \mathcal{L}_{ce} is the binary cross-entropy loss. In this way, the generator loss and the discriminator loss can be summarized as:

$$\begin{aligned} \mathcal{L}_{gen} &= \mathcal{L}_{rec} + \lambda \mathcal{L}_{adv}, \\ \mathcal{L}_{dis} &= \mathcal{L}_{ce}(g_\beta(f_\theta(x, z)), 0) + \mathcal{L}_{ce}(g_\beta(y), 1). \end{aligned} \quad (10)$$

Variational Auto-encoder: For dense prediction task with input variable x and output variable y , we refer to conditional variational auto-encoder (CVAE) [74] instead, where the input image x is the conditional variable. As a conditional directed graph model, a conventional CVAE mainly contains two modules: a generator model $f_\theta(x)$, which is a saliency generator in this paper, to produce the task related predictions, and an inference model $q_\theta(z|x, y)$, which infers the latent variable z with image x and annotation y as input. Learning a CVAE framework involves approximation of the true posterior distribution of z with an inference model $q_\theta(z|x, y)$, with the loss function as:

$$\begin{aligned} \mathcal{L}_{cvae} &= \underbrace{\mathbb{E}_{z \sim q_\theta(z|x, y)} [-\log p_\theta(y|x, z)]}_{\mathcal{L}_{rec}} \\ &\quad + D_{KL}(q_\theta(z|x, y) \parallel p_\theta(z|x)). \end{aligned} \quad (11)$$

The first term is the reconstruction loss and the second is the Kullback-Leibler divergence of prior distribution $p_\theta(z|x)$ and posterior distribution $q_\theta(z|x, y)$, where both of them are usually parameterized by multi-layer perceptron (MLP).

Alternating back-propagation: Alternating back-propagation [104] updates the latent variable and network parameters in an EM-manner. Given the network prediction with the current parameter set, it infers the latent variable by Langevin dynamics based MCMC [27], which is called “Inferential back-propagation” [104]. Given the updated latent variable z , the network parameter set is updated with gradient descent, which is called “Learning back-propagation” [104]. Similar to the VAE [73] or CVAE [74] frameworks, ABP intends to infer z and learn the network parameter θ to minimize the reconstruction loss. Specifically, ABP [104] samples z directly from its posterior distribution with a

2. x' is the early-fused RGB x and depth d feature (see Section 4.3.1).

gradient-based Monte Carlo method, namely Langevin Dynamics [27]:

$$z_{t+1} = z_t + \frac{s_t^2}{2} \left[\frac{\partial}{\partial z} \log p_\theta(y, z_t | x) \right] + s_t \mathcal{N}(0, \mathbf{I}), \quad (12)$$

where $z_0 \sim \mathcal{N}(0, \mathbf{I})$, and the gradient term is defined as:

$$\frac{\partial}{\partial z} \log p_\theta(y, z | x) = \frac{1}{\sigma^2} (y - f_\theta(x, z)) \frac{\partial}{\partial z} f_\theta(x, z) - z. \quad (13)$$

t is the time step for Langevin sampling, s_t is the step size, σ^2 is variance of the inherent labeling noise. As no extra network is involved in the ABP based framework, the final loss function contains only the task-related loss.

Generative model analysis: As no inference model is included in GAN, the distribution of z within GAN is always standard normal distribution $\mathcal{N}(0, \mathbf{I})$, which is less informative. For the CVAE based model, it samples the latent variable from the designed posterior distribution during training, and the distribution gap between the designed posterior and the true distribution leads to posterior collapse issue [108], where the latent variable is independent on the input image, leading to less representative latent space. For the ABP based framework, although it samples from the true posterior distribution via Eq. 12, the task related training is not changed, and our experimental experiences show that the deterministic performance is usually heavily influenced, especially for the conventional CNN backbone based frameworks (see Table 3).

4.5 Inferential GAN

Among the above three types of generative models, we find the GAN based models usually lead to the best performance due to the higher level adversarial loss function \mathcal{L}_{adv} within it. In this paper, we introduce inferential generative adversarial network (iGAN), a new generative model for SOD, where we infer the latent variable within the proposed framework instead of defining it as fixed $\mathcal{N}(0, \mathbf{I})$. Specifically, the proposed iGAN infers the latent variable by gradient-based Markov chain Monte Carlo (MCMC), namely Langevin dynamics [27] (see Fig. 6) following ABP, leading to an image conditioned prior distribution. Following the previous variable definitions, given the training example (x, y) , we intend to infer z and learn the network parameters θ to minimize the reconstruction loss as well as a regularization term that corresponds to the prior on z . Our iGAN based framework then include three main parts: a generator for task related predictions, a discriminator to distinguish the prediction and ground truth, and a inference model via Langevin dynamics [27] to infer the latent variable with gradient based MCMC. Different from the isotropic Gaussian distribution assumption for the latent variable in GAN [26], or the possible posterior issue [108] within VAE [73], our latent variable is sampled directly from its real posterior distribution via gradient based MCMC following [104]. Further, we introduce extra adversarial loss and the fully convolutional discriminator, serving as higher order loss function for accurate deterministic predictions. Empirically, we set $s_t = 0.1$ and $\sigma^2 = 0.3$ in Eq. 12 and Eq. 13. During training, we sample z_0 from $\mathcal{N}(0, \mathbf{I})$, and update z via Eq. 12 by running $T = 5$ steps of Langevin sampling [27], and the final z_T is then used to generate saliency prediction in our case. For testing, we can sample directly from the prior distribution of z , which is $\mathcal{N}(0, \mathbf{I})$.

Network Details: The proposed iGAN can be applied to any deterministic saliency detection model, and we show the flowchart

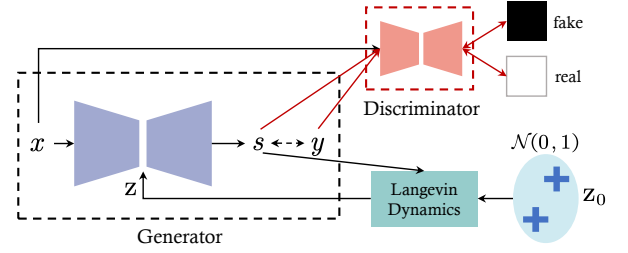


Fig. 6. Flowchart of the proposed inferential GAN. The “Generator” takes image x and latent variable z as input, and generate saliency map s , where the latent variable z is updated via Langevin dynamics based MCMC [27]. The fully convolutional “Discriminator” is designed to distinguish prediction (fake) and ground truth (real).

of the proposed iGAN for saliency detection in Fig. 6. Specifically, we first extend the latent variable z to the same spatial size as the highest level backbone feature (t_4 in this paper). Then we concatenate z with t_4 channel-wise, and feed it to a 3×3 convolutional layer, which will serve as the new t_4 for saliency prediction in Eq. 5. The discriminator contains four 3×3 convolutional layers following batch normalization and leakyReLU activation function with 64 channels, which takes the concatenation of image and model prediction (or ground truth) as input to estimate its pixel-wise realism. In this way, the discriminator loss in Eq. 10 can be rewritten as:

$$\begin{aligned} \mathcal{L}_{dis} = & \mathcal{L}_{ce}(g_\beta(\text{concat}\{f_\theta(x, z), x\}), 0) \\ & + \mathcal{L}_{ce}(g_\beta(\text{concat}\{y, x\}), 1). \end{aligned} \quad (14)$$

The training of the proposed iGAN is the same as the conventional GAN based models in Eq. 10.

5 EXPERIMENTS SETUP

Dataset: In this paper, we conduct research on SOD, including both RGB image-based SOD and RGB-D image pair-based SOD. For the former, we perform fully and weakly supervised saliency detection. Within the fully supervised learning frameworks, we train the models by using the DUTS training dataset [6] $D1 = \{x_i, y_i\}_{i=1}^N$ of size $N = 10,553$, and test on six other widely used datasets: the DUTS testing dataset, ECSSD [109], DUT [11], HKU-IS [17], PASCAL-S [110] and the SOD testing dataset [111]. For weakly supervised models, we use the DUTS-S training dataset [5] $D2 = \{x_i, y_i\}_{i=1}^N$ of size $N = 10,553$, where y_i is scribble annotation instead of pixel-wise annotation in $D1$. We use the same testing dataset for models related to the two different settings.

For RGB-D SOD, we follow the conventional training setting, in which the training set $D3 = \{x_i, y_i\}_{i=1}^N$ is a combination of 1,485 images from the NJU2K dataset [112] and 700 images from the NLPR dataset [115]. We then test the performance of our model and competing models on the NJU2K testing set, NLPR testing set, LFS [116], DES [114], SSB [113] and SIP [117] dataset.

Evaluation Metrics: For all the three tasks, we use four evaluation indicators to measure the performance, including Mean Absolute Error \mathcal{M} , Mean F-measure (F_β), Mean E-measure (E_ϵ) [118] and S-measure (S_α) [119].

MAE \mathcal{M} is defined as the pixel-wise difference between the predicted c and the pixel-wise binary ground-truth y :

$$\text{MAE} = \frac{1}{H \times W} |c - y|, \quad (15)$$

TABLE 1

Baseline model performance, where B_cnn and B_tr are models with CNN and transformer backbones respectively using a binary cross-entropy loss function, B'_cnn and B'_tr are the corresponding models with the structure-aware loss function in Eq. 6.

Method	DUTS [6]				ECSSD [109]				DUT [11]				HKU-IS [17]				PASCAL-S [110]				SOD [111]			
	$S_\alpha \uparrow$	$F_\beta \uparrow$	$E_\xi \uparrow$	$\mathcal{M} \downarrow$	$S_\alpha \uparrow$	$F_\beta \uparrow$	$E_\xi \uparrow$	$\mathcal{M} \downarrow$	$S_\alpha \uparrow$	$F_\beta \uparrow$	$E_\xi \uparrow$	$\mathcal{M} \downarrow$	$S_\alpha \uparrow$	$F_\beta \uparrow$	$E_\xi \uparrow$	$\mathcal{M} \downarrow$	$S_\alpha \uparrow$	$F_\beta \uparrow$	$E_\xi \uparrow$	$\mathcal{M} \downarrow$	$S_\alpha \uparrow$	$F_\beta \uparrow$	$E_\xi \uparrow$	$\mathcal{M} \downarrow$
B_cnn	.878	.818	.895	.042	.922	.907	.937	.039	.822	.724	.834	.061	.912	.886	.933	.035	.862	.838	.891	.067	.831	.808	.846	.079
B'_cnn	.882	.840	.916	.037	.922	.919	.947	.035	.823	.742	.851	.057	.912	.901	.947	.030	.855	.841	.896	.065	.832	.825	.863	.073
B_tr	.907	.863	.930	.031	.939	.929	.957	.028	.858	.786	.878	.051	.929	.912	.954	.027	.881	.866	.911	.056	.854	.841	.882	.065
B'_tr	.911	.882	.947	.026	.939	.940	.965	.024	.860	.801	.894	.045	.927	.921	.964	.023	.876	.872	.917	.053	.858	.853	.897	.059

TABLE 2

Depth contribution analysis for RGB-D SOD. Given the RGB image based model ("*_RGB"), we first adapt it for RGB-D saliency detection with early-fusion ("*Early"). Then, the auxiliary depth estimation module is attached to "*Early" to analyse the depth contribution.

Method	NJU2K [112]				SSB [113]				DES [114]				NLPR [115]				LFSD [116]				SIP [117]			
	$S_\alpha \uparrow$	$F_\beta \uparrow$	$E_\xi \uparrow$	$\mathcal{M} \downarrow$	$S_\alpha \uparrow$	$F_\beta \uparrow$	$E_\xi \uparrow$	$\mathcal{M} \downarrow$	$S_\alpha \uparrow$	$F_\beta \uparrow$	$E_\xi \uparrow$	$\mathcal{M} \downarrow$	$S_\alpha \uparrow$	$F_\beta \uparrow$	$E_\xi \uparrow$	$\mathcal{M} \downarrow$	$S_\alpha \uparrow$	$F_\beta \uparrow$	$E_\xi \uparrow$	$\mathcal{M} \downarrow$	$S_\alpha \uparrow$	$F_\beta \uparrow$	$E_\xi \uparrow$	$\mathcal{M} \downarrow$
CB_RGB	.906	.891	.936	.038	.903	.882	.933	.039	.908	.890	.936	.025	.916	.891	.948	.025	.802	.777	.833	.105	.874	.862	.913	.052
CEarly	.912	.901	.941	.036	.903	.881	.934	.038	.932	.921	.964	.018	.914	.886	.945	.026	.830	.804	.858	.082	.878	.864	.914	.050
CADE	.911	.902	.939	.036	.902	.877	.936	.039	.935	.922	.968	.018	.922	.896	.951	.025	.860	.848	.899	.069	.888	.880	.925	.045
TB_RGB	.924	.919	.955	.029	.922	.906	.952	.030	.918	.908	.943	.022	.931	.914	.962	.021	.869	.856	.899	.067	.895	.898	.935	.042
TEarly	.925	.917	.955	.028	.911	.890	.948	.033	.938	.926	.974	.016	.935	.916	.965	.019	.875	.862	.903	.060	.897	.895	.938	.039
TADE	.925	.917	.953	.029	.911	.890	.946	.034	.944	.930	.977	.015	.934	.913	.965	.018	.879	.869	.910	.056	.902	.895	.939	.038

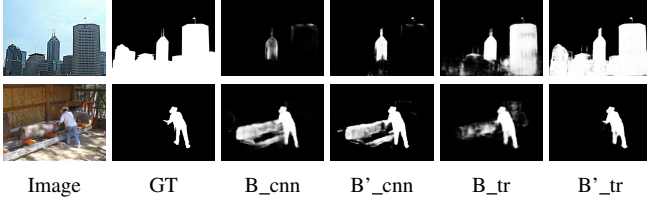


Fig. 7. Predictions of CNN and transformer backbone models without (B_cnn and B_tr) and with (B'_cnn and B'_tr) structure-aware loss.

where H and W are the height and width of c correspondingly.

F-measure F_β is a region-based similarity metric, and we provide the mean F-measure using varying fixed (0-255) thresholds.

E-measure E_ξ is the recently proposed Enhanced alignment measure [118] in the binary map evaluation field to jointly capture image-level statistics and local pixel matching information.

S-measure S_α is a structure based measure [119], which combines the region-aware (S_r) and object-aware (S_o) structural similarity as their final structure metric:

$$S_\alpha = \alpha S_o + (1 - \alpha) S_r, \quad (16)$$

where $\alpha \in [0, 1]$ is the balance parameter and set to 0.5 as default.

6 ACCURATE AND RELIABLE FULLY-SUPERVISED SALIENCY MODEL

6.1 Accurate Saliency Model

In Section 4.1, we discuss that the CNN backbone is not effective in detecting salient object that relies on global context and the stride and pooling operation leads to less accurate structure information of CNN backbone features. We then compare performance of CNN backbone (B_cnn with ResNet50 [19] backbone) and transformer backbone model (B_tr with Swin transformer backbone [24]) for RGB image based SOD, and show performance in Table 1, where the models share the same decoder³. We also visualize predictions from the two different backbone networks in

3. We adjust the decoder accordingly to the backbone features.

Fig. 7 with the structure-aware loss function [2] in Eq. 6 and the conventional binary cross-entropy loss function. The significant performance gap between the two different backbones (B_cnn and B_tr) indicates the superiority of transformer backbone for SOD. Further, we observe, although the transformer has encoded accurate structure information, the structure-aware loss function (B'_tr) that penalizes wrong prediction along object boundaries can lead to more accurate predictions (see Table 1 and Fig. 7).

6.1.1 Effectiveness of Transformer Backbone for Large Salient Object Detection

We want to identify samples where the transformer backbone outperforms the CNN backbone. To do so, we visualize the performance (mean absolute error, MAE) of CNN backbone (B'_cnn) and transformer backbone (B'_tr) w.r.t. size of the salient foreground in Fig. 9. Specifically, we uniformly group the scale of salient foreground to 10 bins, and compute the mean performance of each backbone based model. Fig. 9 shows that the transformer backbone based model outperforms the CNN backbone based model almost consistently across all scales. Specifically, the performance gap for the largest foreground scale (on the DUT [11] and SOD datasets [111]) is the most significant compared with other scales, which explains the superiority of transformer for large salient object detection. There also exist scales for the HKU-IS [17] and PASCAL-S [110] datasets when the transformer backbone based model fails to outperform the CNN backbone based model, which are mainly due to the “double-edged sword” effect of the transformer’s larger receptive field, which will be explained in Section 8. Images in ECSSD dataset [109] are relatively simpler compared with other datasets, and the foreground objects are distributed compactly around image center, leading to less significant performance gain with the transformer backbone.

6.1.2 Effectiveness of Auxiliary Depth Estimation

We discuss also in Section 4.1 that the inconsistent depth contrast distribution leads to different levels of depth contribution for RGB-D SOD. To solve the issue, we present an auxiliary depth estimation module to fully explore the depth contribution. To verify the proposed auxiliary depth estimation module, we design

TABLE 3

Reliable fully-supervised RGB SOD models, where we present performance of stochastic saliency prediction models via GAN, CVAE, ABP as well as the proposed iGAN. Performance of the baseline deterministic models (B'_cnn and B'_tr in Table 1) are listed for easier reference.

	DUTS [6]				ECSSD [109]				DUT [11]				HKU-IS [17]				PASCAL-S [110]				SOD [111]			
Method	$S_\alpha \uparrow$	$F_\beta \uparrow$	$E_\xi \uparrow$	$\mathcal{M} \downarrow$	$S_\alpha \uparrow$	$F_\beta \uparrow$	$E_\xi \uparrow$	$\mathcal{M} \downarrow$	$S_\alpha \uparrow$	$F_\beta \uparrow$	$E_\xi \uparrow$	$\mathcal{M} \downarrow$	$S_\alpha \uparrow$	$F_\beta \uparrow$	$E_\xi \uparrow$	$\mathcal{M} \downarrow$	$S_\alpha \uparrow$	$F_\beta \uparrow$	$E_\xi \uparrow$	$\mathcal{M} \downarrow$	$S_\alpha \uparrow$	$F_\beta \uparrow$	$E_\xi \uparrow$	$\mathcal{M} \downarrow$
CGAN	.881	.839	.917	.036	.919	.916	.945	.036	.818	.734	.845	.056	.909	.898	.945	.031	.857	.845	.899	.064	.818	.807	.846	.078
CCVAE	.877	.833	.911	.040	.922	.920	.949	.034	.817	.735	.845	.063	.910	.900	.947	.031	.855	.842	.897	.066	.830	.822	.866	.073
CABP	.828	.757	.859	.058	.887	.877	.913	.055	.778	.670	.801	.078	.878	.855	.913	.047	.810	.782	.845	.094	.773	.744	.799	.102
CIGAN	.876	.820	.906	.042	.923	.913	.945	.037	.823	.733	.848	.061	.911	.892	.943	.034	.856	.836	.893	.068	.833	.816	.862	.075
B'_cnn	.882	.840	.916	.037	.922	.919	.947	.035	.823	.742	.851	.057	.912	.901	.947	.030	.855	.841	.896	.065	.832	.825	.863	.073
TGAN	.907	.877	.944	.029	.939	.938	.964	.025	.852	.789	.882	.051	.927	.920	.963	.024	.878	.872	.918	.053	.855	.849	.894	.061
TCVAE	.908	.879	.945	.028	.940	.940	.966	.024	.857	.796	.890	.048	.927	.922	.964	.024	.876	.871	.918	.054	.858	.854	.898	.060
TABP	.910	.878	.944	.028	.942	.940	.966	.024	.860	.799	.891	.048	.929	.922	.964	.024	.879	.870	.918	.054	.860	.858	.897	.061
TIGAN	.909	.873	.941	.028	.941	.936	.964	.025	.861	.796	.890	.047	.929	.918	.962	.025	.879	.869	.916	.054	.861	.854	.894	.060
B'_tr	.911	.882	.947	.026	.939	.940	.965	.024	.860	.801	.894	.045	.927	.921	.964	.023	.876	.872	.917	.053	.858	.853	.897	.059

TABLE 4

Reliable fully-supervised RGB-D SOD models, where we present performance of stochastic saliency prediction models via GAN, CVAE, ABP as well as the proposed iGAN. Performance of the baseline models (CADE and TADE in Table 2) are listed for easier reference.

	NJU2K [112]				SSB [113]				DES [114]				NLPR [115]				LFSD [116]				SIP [117]			
Method	$S_\alpha \uparrow$	$F_\beta \uparrow$	$E_\xi \uparrow$	$\mathcal{M} \downarrow$	$S_\alpha \uparrow$	$F_\beta \uparrow$	$E_\xi \uparrow$	$\mathcal{M} \downarrow$	$S_\alpha \uparrow$	$F_\beta \uparrow$	$E_\xi \uparrow$	$\mathcal{M} \downarrow$	$S_\alpha \uparrow$	$F_\beta \uparrow$	$E_\xi \uparrow$	$\mathcal{M} \downarrow$	$S_\alpha \uparrow$	$F_\beta \uparrow$	$E_\xi \uparrow$	$\mathcal{M} \downarrow$	$S_\alpha \uparrow$	$F_\beta \uparrow$	$E_\xi \uparrow$	$\mathcal{M} \downarrow$
CGAN	.914	.905	.943	.035	.904	.881	.937	.039	.929	.917	.957	.019	.924	.899	.954	.023	.849	.826	.884	.074	.885	.875	.921	.047
CCVAE	.906	.894	.937	.039	.896	.871	.934	.041	.940	.923	.975	.017	.916	.891	.951	.026	.841	.825	.881	.075	.887	.878	.927	.045
CABP	.916	.903	.941	.034	.905	.878	.935	.039	.941	.928	.972	.017	.921	.891	.949	.025	.845	.828	.876	.077	.888	.876	.922	.046
CIGAN	.914	.900	.939	.036	.903	.876	.934	.040	.937	.921	.970	.018	.922	.890	.952	.025	.851	.832	.889	.075	.884	.870	.917	.049
CADE	.911	.902	.939	.036	.902	.877	.936	.039	.935	.922	.968	.018	.922	.896	.951	.025	.860	.848	.899	.069	.888	.880	.925	.045
TGAN	.928	.921	.956	.027	.911	.890	.946	.034	.941	.931	.975	.015	.934	.915	.964	.019	.875	.860	.903	.060	.900	.901	.939	.038
TCVAE	.928	.922	.956	.028	.911	.889	.944	.035	.941	.929	.973	.016	.935	.915	.964	.020	.879	.863	.905	.060	.903	.904	.941	.038
TABP	.927	.917	.954	.029	.913	.891	.947	.034	.943	.929	.974	.015	.933	.911	.962	.020	.870	.852	.900	.065	.904	.900	.942	.037
TIGAN	.928	.919	.956	.028	.915	.893	.947	.034	.940	.929	.970	.016	.932	.911	.961	.020	.884	.868	.911	.057	.905	.901	.941	.037
TADE	.925	.917	.953	.029	.911	.890	.946	.034	.944	.930	.977	.015	.934	.913	.965	.018	.879	.869	.910	.056	.902	.895	.939	.038

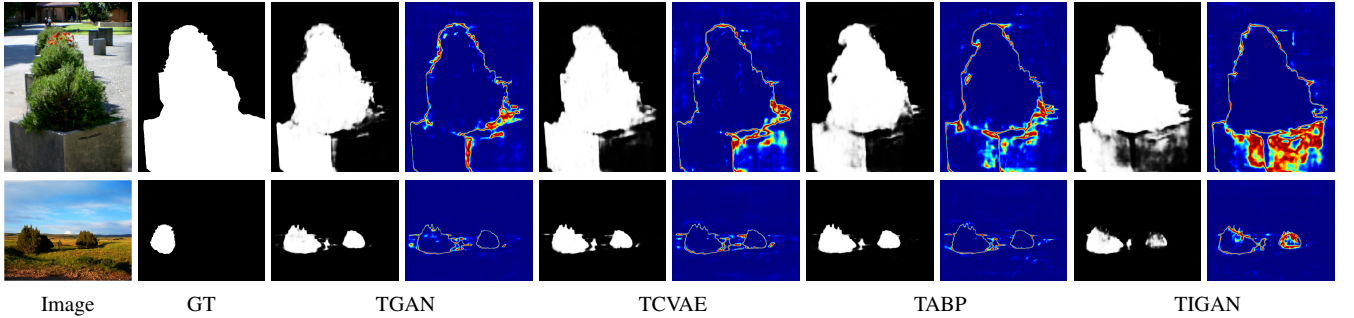


Fig. 8. Predictions from different generative models in Table 3, where we random sample $T = 10$ times and obtain the entropy of mean prediction as predictive uncertainty [28]. Note that the predictions within each method block are saliency prediction and uncertainty respectively.

three SOD models, namely the pure RGB image based model (“CB_RGB” and “TB_RGB”), early fusion model (“CEarly” and “TEarly”) and early fusion model with auxiliary depth estimation module (“CADE” and “TADE”), where “C*” is the CNN backbone (ResNet50 [19]) based model and “T*” is the transformer backbone based model. The performance of each model is shown in Table 2. We observe on average improved performance of early fusion models compared with training only with RGB image, indicating the benefits of depth for SOD. Further, as shown in Fig. 3, salient foreground depth contrast of LFSD dataset [116] is most different from the corresponding RGB image salient foreground contrast. In this way, we claim the auxiliary depth estimation should contribute the most, which is consistent with our experiments. Note that, the proposed auxiliary depth estimation module aims to further explore the depth contribution, especially for depth data that shares more complementary information with the RGB image (see Section 4.1 and Fig. 3).

6.2 Reliable Saliency Model

Model reliability is an important factor for measuring the accountability for decisions before deployment, and a reliable model should be aware of its predictions. In this paper, we introduce the iGAN for reliable saliency detection with an image conditioned latent prior. In addition to the proposed iGAN, we also design GAN-based [26], CVAE-based [73], [74] and ABP-based [104] generative models for RGB SOD and RGB-D SOD. The performance is shown in Table 3 and Table 4 respectively, where “CGAN”, “CCVAE”, “CABP” and “CIGAN” are the stochastic models based on GAN, CVAE, ABP and the proposed inferential GAN respectively with CNN backbone, and “TGAN”, “TCVAE”, “TABP” and “TIGAN” are the transformer counterparts. Note that, for the CVAE [74] based models, we follow the same prior and posterior distribution model designing as in [120].

For easier reference, we also list the baseline models B'_cnn and B'_tr from Table 1 in Table 3, and the CNN and transformer

TABLE 5
Weakly-supervised SOD analysis with both the CNN and transformer backbone.

Method	DUTS [6]				ECSSD [109]				DUT [11]				HKU-IS [17]				PASCAL-S [110]				SOD [111]			
	$S_\alpha \uparrow$	$F_\beta \uparrow$	$E_\xi \uparrow$	$\mathcal{M} \downarrow$	$S_\alpha \uparrow$	$F_\beta \uparrow$	$E_\xi \uparrow$	$\mathcal{M} \downarrow$	$S_\alpha \uparrow$	$F_\beta \uparrow$	$E_\xi \uparrow$	$\mathcal{M} \downarrow$	$S_\alpha \uparrow$	$F_\beta \uparrow$	$E_\xi \uparrow$	$\mathcal{M} \downarrow$	$S_\alpha \uparrow$	$F_\beta \uparrow$	$E_\xi \uparrow$	$\mathcal{M} \downarrow$	$S_\alpha \uparrow$	$F_\beta \uparrow$	$E_\xi \uparrow$	$\mathcal{M} \downarrow$
BCNN	.754	.641	.806	.088	.822	.771	.868	.087	.723	.588	.758	.107	.807	.739	.864	.080	.760	.703	.812	.117	.745	.692	.801	.117
BCNN_S	.805	.724	.858	.069	.869	.846	.913	.060	.771	.664	.806	.088	.859	.822	.913	.055	.802	.768	.855	.095	.780	.750	.841	.098
BCNN_G	.835	.781	.884	.053	.895	.889	.934	.046	.796	.708	.831	.068	.883	.871	.932	.041	.825	.807	.874	.080	.797	.787	.843	.070
BCNN_self	.787	.682	.834	.077	.851	.803	.888	.075	.761	.634	.793	.089	.833	.767	.880	.072	.796	.743	.839	.100	.766	.716	.811	.111
BCNN_weak	.839	.792	.892	.050	.895	.892	.934	.044	.800	.719	.835	.063	.886	.877	.935	.039	.829	.813	.880	.078	.788	.778	.834	.088
BT	.748	.636	.798	.081	.834	.786	.885	.071	.728	.600	.765	.099	.802	.734	.861	.077	.777	.727	.830	.100	.756	.710	.820	.108
BT_S	.829	.767	.893	.053	.886	.878	.938	.045	.807	.726	.854	.069	.869	.848	.932	.046	.825	.810	.884	.078	.802	.791	.869	.085
BT_G	.857	.808	.916	.043	.908	.903	.951	.036	.825	.751	.870	.059	.896	.883	.949	.035	.843	.831	.898	.069	.819	.813	.877	.077
BT_self	.791	.683	.840	.070	.854	.799	.893	.069	.773	.649	.809	.083	.832	.763	.882	.070	.802	.748	.846	.094	.781	.732	.836	.101
BT_weak	.858	.815	.917	.042	.908	.907	.952	.035	.835	.770	.879	.054	.898	.891	.952	.034	.848	.843	.904	.065	.821	.819	.880	.075

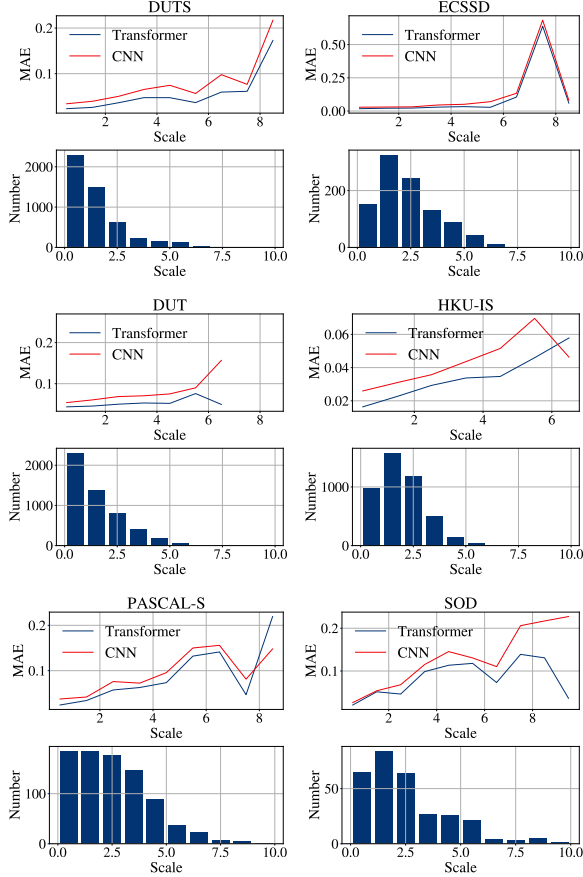


Fig. 9. Model (B'_cnn and B'_tr in Table 1) performance (the top curve of each block) w.r.t. salient foreground size distribution (the bottom bar of each block) on six testing datasets.

backbone based stochastic models are built upon the two baseline models respectively. The stochastic RGB-D SOD models in Table 4 are based on the corresponding RGB-D SOD models with auxiliary depth estimation module as shown in Table 2. We show performance of “CADE” and “TADE” for easier reference. Table 3 and Table 4 show that the four types of generative models can achieve comparable deterministic performance (compared with the corresponding deterministic baseline models) for both RGB image based SOD and RGB-D image pair based SOD. As the goal of a generative model is to obtain stochastic predictions for model explanation, the deterministic performance may be slightly influenced, *e.g.* “CABP” for RGB SOD. The main reason lies in

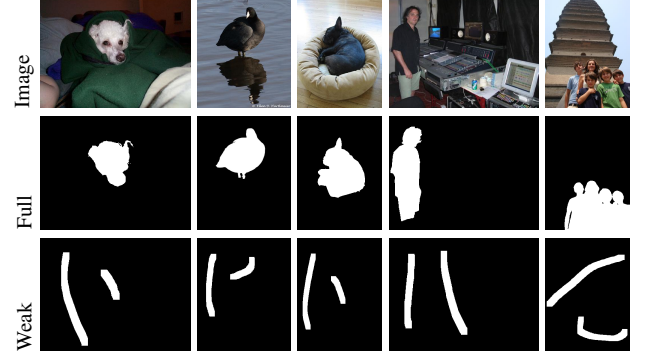


Fig. 10. The scribble (“Weak”) and the full annotations (“Full”).

two parts. Firstly, the hyper-parameters within the inference model in Eq. (12) need to be well-tuned to effectively explore the latent space. Secondly, the final performances of those generative models are obtained by performing multiple iterations (10 iterations in this paper) of forward passes during testing, and performance of the mean prediction is then reported, which varies with different iterations of sampling. In this paper, we focus on the new generative model for accurate and reliable SOD, we will leave the generative model hyper-parameter tuning for the future work.

Besides the deterministic performance, the main advantage of generative model is its ability for stochastic predictions, making it possible to estimate predictive uncertainty [28] for model reliability estimation. In Fig. 8, we visualize the uncertainty maps of each generative model. In this paper, the “uncertainty” refers to predictive uncertainty [28], [121], which is the total uncertainty, including both data uncertainty and model uncertainty. Given the mean predictions after multiple forward passes during testing, the predictive uncertainty is defined as entropy of the mean prediction. A reliable model should be aware of its prediction, leading to a reasonable uncertainty model to explain model prediction. Fig. 8 shows that the uncertainty map from the proposed inferential GAN explains better model prediction, which highlights both the hard samples (data uncertainty, image in the 1st row) and out-of-distribution samples (model uncertainty, image in the 2nd row).

7 ACCURATE AND RELIABLE WEAKLY-SUPERVISED SALIENCY MODEL

Different from pixel-wise annotation based fully supervised SOD, weakly supervised SOD models learn saliency from cheap annotations, *e.g.*, scribble annotations [5], image-level labels [6]. In this

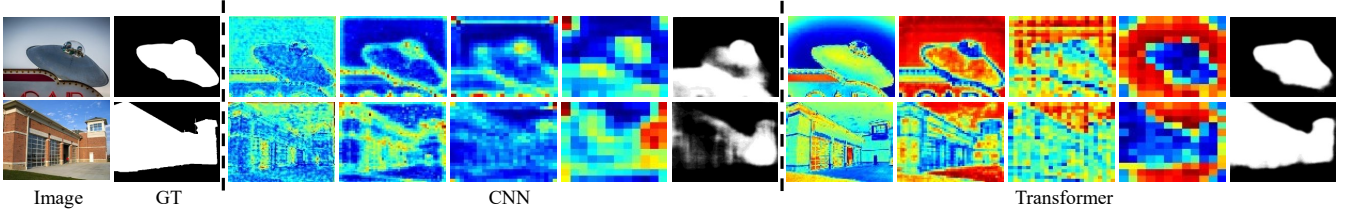


Fig. 11. Features of CNN (ResNet50 [19]) and transformer backbone (Swin [24]) for weakly-supervised SOD using only partial cross-entropy loss.

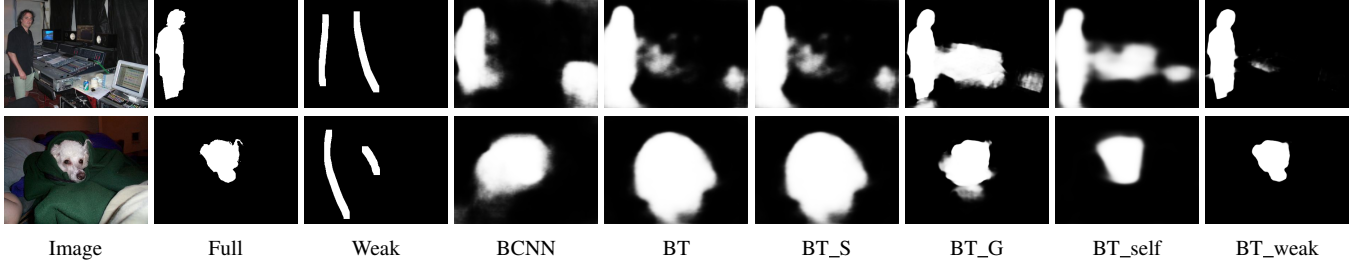


Fig. 12. Weakly supervised saliency model predictions with different loss functions. Detailed performance of each model is illustrated in Table 5.

TABLE 6

Reliable weakly-supervised RGB SOD models, where the deterministic models ("**_weak") is the proposed deterministic weakly-supervised SOD model with loss function in Eq. 18.

Method	DUTS [6]				ECSSD [109]				DUT [11]				HKU-IS [17]				PASCAL-S [110]				SOD [111]			
	$S_{\alpha} \uparrow$	$F_{\beta} \uparrow$	$E_{\xi} \uparrow$	$\mathcal{M} \downarrow$	$S_{\alpha} \uparrow$	$F_{\beta} \uparrow$	$E_{\xi} \uparrow$	$\mathcal{M} \downarrow$	$S_{\alpha} \uparrow$	$F_{\beta} \uparrow$	$E_{\xi} \uparrow$	$\mathcal{M} \downarrow$	$S_{\alpha} \uparrow$	$F_{\beta} \uparrow$	$E_{\xi} \uparrow$	$\mathcal{M} \downarrow$	$S_{\alpha} \uparrow$	$F_{\beta} \uparrow$	$E_{\xi} \uparrow$	$\mathcal{M} \downarrow$	$S_{\alpha} \uparrow$	$F_{\beta} \uparrow$	$E_{\xi} \uparrow$	$\mathcal{M} \downarrow$
CGAN	.834	.785	.887	.053	.891	.888	.932	.046	.792	.706	.826	.069	.881	.873	.933	.041	.828	.814	.880	.079	.798	.797	.852	.082
CCVAE	.832	.781	.882	.055	.894	.889	.934	.045	.793	.708	.827	.070	.883	.872	.933	.041	.822	.806	.876	.081	.797	.792	.851	.085
CABP	.838	.790	.893	.051	.894	.890	.935	.044	.801	.718	.838	.064	.887	.878	.937	.039	.828	.813	.882	.078	.794	.791	.848	.084
CIGAN	.834	.779	.887	.056	.896	.890	.938	.044	.799	.713	.838	.070	.886	.873	.938	.039	.827	.810	.880	.079	.800	.793	.855	.083
BCNN_weak	.839	.792	.892	.050	.895	.892	.934	.044	.800	.719	.835	.063	.886	.877	.935	.039	.829	.813	.880	.078	.788	.778	.834	.088
TGAN	.856	.813	.918	.043	.906	.905	.950	.037	.824	.753	.868	.060	.895	.886	.949	.035	.848	.840	.905	.065	.819	.816	.878	.076
TCVAE	.855	.813	.916	.043	.907	.906	.950	.036	.825	.757	.872	.059	.894	.887	.949	.035	.843	.837	.900	.067	.814	.813	.873	.079
TABP	.854	.812	.917	.043	.905	.905	.951	.036	.827	.759	.875	.058	.893	.887	.950	.035	.847	.844	.906	.064	.810	.810	.868	.082
TIGAN	.855	.814	.918	.043	.905	.905	.950	.037	.826	.760	.874	.058	.893	.887	.949	.035	.844	.839	.902	.066	.811	.810	.872	.082
BT_weak	.858	.815	.917	.042	.908	.907	.952	.035	.835	.770	.879	.054	.898	.891	.952	.034	.848	.843	.904	.065	.821	.819	.880	.075

paper, we investigate the superiority of the transformer backbone for weakly supervised SOD with scribble supervision [5].

7.1 Weakly-supervised Transformer

The main difficulty of learning from weak annotations is the missing structure information, which cannot be recovered without extra structure-aware regularizers. In Fig. 10, we visualize the weak label (scribble annotation) and full label (pixel-wise annotation), which clearly indicates the missing structure attributes of the weak annotation. In this way, the main focus of designing models to learn from weak annotations is to recover the missing structure information. Specifically, we investigate three widely used strategies, namely smoothness loss [122], gated CRF loss [100], and data-augmentation based consistency loss. The first and second ones aim to recover the structure of prediction, and the third one aims to achieve transformation robust prediction, serving as internal data augmentation trick. To test how model performs with different loss functions within both the CNN framework and the transformer framework, we design models with each type of loss function within both the CNN backbone and transformer backbone, and show performance in Table 5.

Implementation details: To train the weakly-supervised transformer for SOD, similar to [5], we adopt extra smoothness

loss [122] \mathcal{L}_{sm} , the gated CRF loss [100] \mathcal{L}_{gcrf} and the data-augmentation based self-supervised learning strategy [96] \mathcal{L}_{ss} to recover the missing structure information in scribble annotation. The smoothness loss aims to produce a saliency map with edges well-aligned with the input image. The gated CRF loss introduces pair-wise constraints to produce a saliency map with spatial consistency. The self-supervised learning strategy aims to achieve transformation robust predictions. For the Swin transformer backbone [24], as it can only take fixed size input, we perform image rotation instead of image scaling to achieve data augmentation. Specifically, we define the self-supervised loss as a weighted sum of the structural similarity index measure [107] and L_1 loss, which is defined as:

$$\mathcal{L}_{ss} = \alpha * SSIM(s, s^t) + (1 - \alpha) * L_1(s, s^t), \quad (17)$$

where $s = f_{\theta}(T(x))$ is the output of the generator with the rotated image $T(x)$ as input, and $s^t = T(f_{\theta}(x))$ is the rotated prediction with original image x as input. We randomly pick the rotation $T(\cdot)$ from $\{\pi, 1/2\pi, -1/2\pi\}$ in our experiments. α is used to balance the two types of loss functions and we set $\alpha = 0.85$ in our experiments following [96]. Further, given the scribble annotation, we adopt the partial cross-entropy loss \mathcal{L}_{pce}



Fig. 13. Predictions of reliable weakly-supervised transformer.

to constrain predictions on the scribble region. In this way, we define the loss function for the weakly-supervised model as:

$$\mathcal{L}_{weak} = \mathcal{L}_{pce} + \lambda_1 * \mathcal{L}_{sm} + \lambda_2 * \mathcal{L}_{gcrf} + \lambda_3 * \mathcal{L}_{ss}. \quad (18)$$

With grid search, we set $\lambda_1 = 0.3$, $\lambda_2 = 1.0$ and $\lambda_3 = 1.2$.

CNN backbone vs Transformer backbone: We design two different models with ResNet50 [19] and Swin transformer [24] as backbone. The decoder part is the same as B'_tr in Table 1. We train the two models with only partial cross-entropy loss, and we show their corresponding results in Table 5 “BCNN” and “BT” respectively. The significantly better performance of “BT” compared with “BCNN” shows the effectiveness of the transformer backbone for weakly-supervised SOD. We also visualize the features of the two trained models in Fig. 11, where heat maps are the features and binary maps are the predictions. We observe clear structure information in “Transformer”, which explains the superior performance of the transformer for weakly-supervised learning via supervisions with less structure information [123].

Weakly-supervised loss analysis: Beside the partial cross-entropy loss, we use three extra loss functions for weakly-supervised SOD, namely smoothness loss to constrain the predictions to be well aligned with the image edges, gated CRF loss to regularize the pairwise term predictions which aims to produce similar predictions for spatially similar pixels, and a self-supervised loss to effectively learn from less supervision data with consistency loss, *e.g.*, rotation-invariant predictions. We then carried out extra experiments to verify the effectiveness of each loss function, and show the results in Table 5. “BCNN_S”, “BCNN_G” and “BCNN_self” indicate baseline model (“BCNN”) training with extra smoothness loss “ \mathcal{L}_{sm} ”, gated CRF loss “ \mathcal{L}_{gcrf} ” and self-supervised loss “ \mathcal{L}_{ss} ”. “BT_S”, “BT_G” and “BT_self” are the corresponding transformer backbone counterparts. We observe improved performance of each extra loss function, which explains the effectiveness of them. Further, we find that the smoothness and gated CRF achieve more performance gain than the self-supervised loss, which mainly comes from their effective structure modeling ability. The improved performance of BCNN_weak and BT_weak with the weighted loss function in Eq. 18 compared with the corresponding models with individual loss functions verifies the effectiveness of the proposed weighted weakly supervised loss function. We also show predictions of the weakly supervised models in Fig. 12. It is clear that both the base model with only partial cross-entropy loss (“BCNN” and “BT”) and the model with extra self-supervised loss (“BT_self”) fail to accurately localize object boundaries, leading to blurred predictions. The main reason is the absent of structure constraints. The smoothness loss and the gated CRF loss work better in modeling the structure

information, leading to more accurate predictions, especially along object boundaries, and models (“BCNN_weak” and “BT_weak”) with our final loss function (Eq. 18) achieve the best performance.

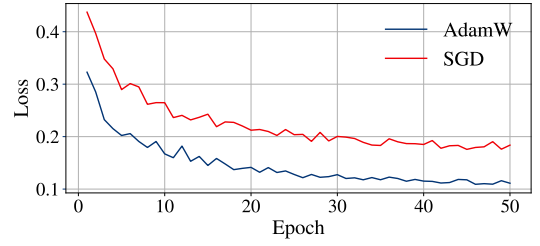


Fig. 14. Loss convergence curves of transformer backbone-based SOD network with AdamW and SGD optimizer.

7.2 Reliable Weakly-supervised Transformer

The generative models for the fully-supervised setting are straightforward, as we can simply take the inferred latent variable as part of the input, and the discriminator can directly estimate real/fake of its input (the ground truth/model prediction). In this section, we apply our proposed inferential GAN to weakly-supervised RGB SOD. We also design the GAN [26], VAE [73], [74] and ABP [104] based generative models for comparison. Similarly, we design the generative model within both CNN backbone and transformer backbone. The performance is shown in Table 6, where “CGAN”, “CCVAE”, “CABP” and “CIGAN” are the stochastic models based on GAN, CVAE, ABP and the proposed inferential GAN respectively with CNN backbone, and “TGAN”, “TCVAE”, “TABP” and “TIGAN” are the corresponding transformer counterparts. Same as the fully-supervised reliable models in Table 3 and Table 4, the prior and posterior distribution models are designed following [120].

Implementation details: For the learning process of reliable weakly-supervised transformer, we apply the same pipeline of the fully supervised method. Considering there are only scribble ground-truth as supervision in training the discriminator, we use partial cross entropy loss for training the discriminator within the GAN and our proposed iGAN based models.

Performance analysis: For easier reference, we also list the baseline models “BCNN_weak” and “BT_weak” from Table 5 in Table 6, and the CNN and transformer backbone based stochastic models are built upon the two baseline models respectively. Same as the results of fully supervised SOD models in Table 3, the three types of generative models for weakly-supervised SOD can also achieve comparable deterministic performance. We further visualize the prediction of the proposed “TIGAN” with uncertainty map in Fig. 13, which explains that the proposed inferential GAN can also achieve accurate and reliable prediction for weakly-supervised saliency prediction.

8 DISCUSSIONS

In this section, we analyse our transformer backbone-based models in detail. Unless otherwise stated, all the following experiments are based on the fully supervised deterministic RGB SOD task (“B'_tr” in Table 1).

Model performance w.r.t. optimizer: We observe that the transformer backbone is sensitive to the optimizer, and the AdamW

TABLE 7

Model analysis related experiments, where we discuss model performance with respect to model optimizer (“B’_SGD” and “B’_trSGD”), initialization weights (“B’_R”, “B’_trR” and “B’_tr22K”) and different transformer backbones (“B’_ViT”).

Method	DUTS [6]				ECSSD [109]				DUT [11]				HKU-IS [17]				PASCAL-S [110]				SOD [111]			
	$S_{\alpha} \uparrow$	$F_{\beta} \uparrow$	$E_{\xi} \uparrow$	$\mathcal{M} \downarrow$	$S_{\alpha} \uparrow$	$F_{\beta} \uparrow$	$E_{\xi} \uparrow$	$\mathcal{M} \downarrow$	$S_{\alpha} \uparrow$	$F_{\beta} \uparrow$	$E_{\xi} \uparrow$	$\mathcal{M} \downarrow$	$S_{\alpha} \uparrow$	$F_{\beta} \uparrow$	$E_{\xi} \uparrow$	$\mathcal{M} \downarrow$	$S_{\alpha} \uparrow$	$F_{\beta} \uparrow$	$E_{\xi} \uparrow$	$\mathcal{M} \downarrow$	$S_{\alpha} \uparrow$	$F_{\beta} \uparrow$	$E_{\xi} \uparrow$	$\mathcal{M} \downarrow$
B’_cnn	.882	.840	.916	.037	.922	.919	.947	.035	.823	.742	.851	.057	.912	.901	.947	.030	.855	.841	.896	.065	.832	.825	.863	.073
B’_SGD	.876	.826	.910	.041	.918	.910	.944	.038	.820	.733	.846	.062	.909	.894	.945	.033	.856	.840	.895	.067	.827	.813	.863	.077
B’_R	.745	.623	.773	.110	.832	.789	.853	.093	.738	.605	.762	.114	.820	.760	.858	.084	.752	.697	.777	.140	.725	.673	.758	.145
B’_tr	.911	.882	.947	.026	.939	.940	.965	.024	.860	.801	.894	.045	.927	.921	.964	.023	.876	.872	.917	.053	.858	.853	.897	.059
B’_trSGD	.899	.861	.936	.031	.928	.923	.954	.032	.854	.786	.886	.046	.921	.909	.956	.029	.867	.856	.905	.061	.833	.818	.862	.075
B’_trR	.768	.667	.804	.097	.848	.819	.874	.082	.754	.637	.784	.105	.843	.803	.884	.070	.760	.715	.794	.134	.730	.689	.763	.142
B’_tr22K	.918	.891	.952	.025	.944	.943	.967	.022	.869	.814	.902	.044	.933	.928	.968	.022	.885	.881	.925	.050	.863	.863	.900	.059
B’_ViT	.922	.899	.955	.023	.943	.945	.967	.022	.874	.824	.906	.043	.934	.931	.969	.021	.884	.884	.926	.050	.858	.859	.895	.065

TABLE 8

Replacing the CNN backbone of existing RGB SOD models with a transformer backbone.

Method	DUTS [6]				ECSSD [109]				DUT [11]				HKU-IS [17]				PASCAL-S [110]				SOD [111]			
	$S_{\alpha} \uparrow$	$F_{\beta} \uparrow$	$E_{\xi} \uparrow$	$\mathcal{M} \downarrow$	$S_{\alpha} \uparrow$	$F_{\beta} \uparrow$	$E_{\xi} \uparrow$	$\mathcal{M} \downarrow$	$S_{\alpha} \uparrow$	$F_{\beta} \uparrow$	$E_{\xi} \uparrow$	$\mathcal{M} \downarrow$	$S_{\alpha} \uparrow$	$F_{\beta} \uparrow$	$E_{\xi} \uparrow$	$\mathcal{M} \downarrow$	$S_{\alpha} \uparrow$	$F_{\beta} \uparrow$	$E_{\xi} \uparrow$	$\mathcal{M} \downarrow$	$S_{\alpha} \uparrow$	$F_{\beta} \uparrow$	$E_{\xi} \uparrow$	$\mathcal{M} \downarrow$
SCRN [1]	.885	.833	.900	.040	.920	.910	.933	.041	.837	.749	.847	.056	.916	.894	.935	.034	.869	.833	.892	.063	.817	.790	.829	.087
F3Net [2]	.888	.852	.920	.035	.919	.921	.943	.036	.839	.766	.864	.053	.917	.910	.952	.028	.861	.835	.898	.062	.824	.814	.850	.077
SCRN* [1]	.908	.873	.937	.029	.937	.935	.960	.027	.864	.800	.890	.044	.930	.919	.958	.026	.875	.870	.911	.057	.843	.836	.865	.069
F3Net* [2]	.913	.891	.950	.024	.939	.941	.965	.023	.860	.802	.891	.042	.928	.925	.964	.023	.872	.872	.916	.055	.848	.849	.881	.065
B’_tr	.911	.882	.947	.026	.939	.940	.965	.024	.860	.801	.894	.045	.927	.921	.964	.023	.876	.872	.917	.053	.858	.853	.897	.059

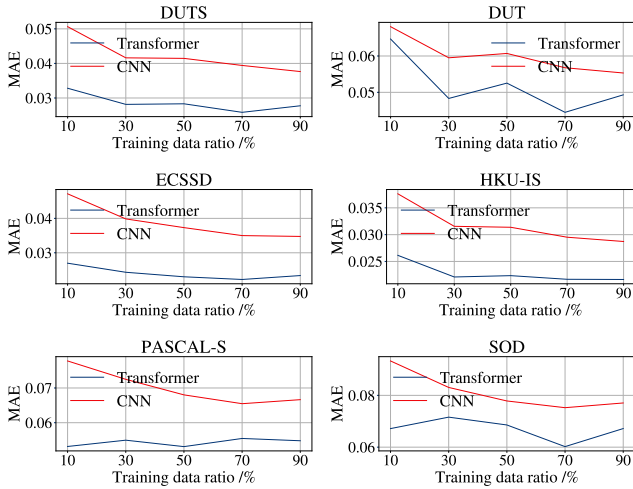


Fig. 15. Model performance of the CNN backbone and the transformer backbone w.r.t. different training dataset sizes on six testing datasets.

optimizer is more suitable to train the transformer backbone (Swin [24] in particularly) based framework compared with SGD. To explain this, we train B’_cnn (CNN backbone model) and B’_tr (transformer backbone model) with SGD as optimizer, leading to B’_SGD and B’_trSGD respectively in Table 7. We observe that for both the CNN and transformer backbone based network, the SGD optimizer usually achieves worse performance compared with the AdamW optimizer. We further visualize the loss convergence curve of transformer backbone based models in Fig. 14. Note that models with the two types of optimizer share the same initial learning rate, and “SGD” in this paper are SGD with momentum of 0.9. We find that after the first epoch, the AdamW optimizer based model jumps directly to a minimum of smaller loss compared with SGD, and later, the loss decrease behaviours of both models are similar. We also tried different learning rate configuration for models with the two types of optimizer, and the

performance of SGD based model is still bad. We further explore whether the AdamW converges faster than SGD. However, even when we train more epochs for SGD based model, the conclusion is still similar. We will investigate it further in the future to extensively explain the different model behaviours with various types of optimizer.

The importance of initialization weights: Note that, for both conventional backbones and our transformer backbone, we initialize them with the image classification model trained on the ImageNet-1K [124] dataset. To test how the initialization weights contribute to the model performance, we randomly initialize the two models (B’_cnn and B’_tr in Table 1) and obtain model performance as B’_R and B’_trR in Table 7. We observe worse performance of both B’_R and B’_trR, which further illustrates the necessity of fine-tuning the backbone models for SOD. We also initialize our transformer backbone with parameters pre-trained on the ImageNet-22K dataset, and show the result as B’_tr22K in Table 7. The better performance of B’_tr22K compared with B’_tr again explains the importance of the initialization weights for the backbone network.

Different transformer backbone analysis: Following our pipeline, we change the Swin transformer backbone [24] to the ViT backbone [23], [29], and achieve B’_ViT in Table 7. Note that, the ViT backbone we used in Table 7 is initialized with weights trained on ImageNet-22K. The comparable performance of B’_ViT compared with B’_tr22K explains that the two types of backbones both work for SOD.

Model performance with different numbers of training datasets: As the two types of backbones (CNN and transformer) have significantly different numbers of model parameters, leading to different model capacities. We aim to analyse how model capacity is sensitive to scales of the training dataset. We then train our transformer backbone networks (B’_tr) and CNN backbone based model (B’_cnn) in Table 1) with different sizes of training datasets, which are 10%, 30%, 50%, 70%, 90% of the entire training dataset respectively, and show model performance in Fig. 15. The consistently better performance of the transformer backbone-

TABLE 9
Performance comparison with benchmark fully-supervised RGB SOD models.

Method	DUTS [6]				ECSSD [109]				DUT [11]				HKU-IS [17]				PASCAL-S [110]				SOD [111]			
	$S_\alpha \uparrow$	$F_\beta \uparrow$	$E_\xi \uparrow$	$\mathcal{M} \downarrow$	$S_\alpha \uparrow$	$F_\beta \uparrow$	$E_\xi \uparrow$	$\mathcal{M} \downarrow$	$S_\alpha \uparrow$	$F_\beta \uparrow$	$E_\xi \uparrow$	$\mathcal{M} \downarrow$	$S_\alpha \uparrow$	$F_\beta \uparrow$	$E_\xi \uparrow$	$\mathcal{M} \downarrow$	$S_\alpha \uparrow$	$F_\beta \uparrow$	$E_\xi \uparrow$	$\mathcal{M} \downarrow$	$S_\alpha \uparrow$	$F_\beta \uparrow$	$E_\xi \uparrow$	$\mathcal{M} \downarrow$
CIGAN	.876	.820	.906	.042	.923	.913	.945	.037	.823	.733	.848	.061	.911	.892	.943	.034	.856	.836	.893	.068	.833	.816	.862	.075
TIGAN	.909	.873	.941	.028	.941	.936	.964	.025	.861	.796	.890	.047	.929	.918	.962	.025	.879	.869	.916	.054	.861	.854	.894	.060
SCRN [1]	.885	.833	.900	.040	.920	.910	.933	.041	.837	.749	.847	.056	.916	.894	.935	.034	.869	.833	.892	.063	.817	.790	.829	.087
F3Net [2]	.888	.852	.920	.035	.919	.921	.943	.036	.839	.766	.864	.053	.917	.910	.952	.028	.861	.835	.898	.062	.824	.814	.850	.077
ITSD [125]	.886	.841	.917	.039	.920	.916	.943	.037	.842	.767	.867	.056	.921	.906	.950	.030	.860	.830	.894	.066	.836	.829	.867	.076
PAKRNet [126]	.900	.876	.935	.033	.928	.930	.951	.032	.853	.796	.888	.050	.923	.919	.955	.028	.859	.856	.898	.068	.833	.836	.866	.074
MSFNet [34]	.877	.855	.927	.034	.915	.927	.951	.033	.832	.772	.873	.050	.909	.913	.957	.027	.849	.855	.900	.064	.813	.822	.852	.077
CTDNet [127]	.893	.862	.928	.034	.925	.928	.950	.032	.844	.779	.874	.052	.919	.915	.954	.028	.861	.856	.901	.064	.829	.832	.858	.074
VST [70]	.896	.842	.918	.037	.932	.911	.943	.034	.850	.771	.869	.058	.928	.903	.950	.030	.873	.832	.900	.067	.854	.833	.879	.065
GTSOD [71]	.908	.875	.942	.029	.935	.935	.962	.026	.858	.797	.892	.051	.930	.922	.964	.023	.877	.855	.915	.054	.860	.860	.898	.061

TABLE 10
Performance comparison with benchmark fully-supervised RGB-D SOD models.

Method	NJU2K [112]				SSB [113]				DES [114]				NLPR [115]				LFSD [116]				SIP [117]			
	$S_\alpha \uparrow$	$F_\beta \uparrow$	$E_\xi \uparrow$	$\mathcal{M} \downarrow$	$S_\alpha \uparrow$	$F_\beta \uparrow$	$E_\xi \uparrow$	$\mathcal{M} \downarrow$	$S_\alpha \uparrow$	$F_\beta \uparrow$	$E_\xi \uparrow$	$\mathcal{M} \downarrow$	$S_\alpha \uparrow$	$F_\beta \uparrow$	$E_\xi \uparrow$	$\mathcal{M} \downarrow$	$S_\alpha \uparrow$	$F_\beta \uparrow$	$E_\xi \uparrow$	$\mathcal{M} \downarrow$	$S_\alpha \uparrow$	$F_\beta \uparrow$	$E_\xi \uparrow$	$\mathcal{M} \downarrow$
CIGAN	.914	.900	.939	.036	.903	.876	.934	.040	.937	.921	.970	.018	.922	.890	.952	.025	.851	.832	.889	.075	.884	.870	.917	.049
TIGAN	.928	.919	.956	.028	.915	.893	.947	.034	.940	.929	.970	.016	.932	.911	.961	.020	.884	.868	.911	.057	.905	.901	.941	.037
BBSNet [4]	.921	.902	.938	.035	.908	.883	.928	.041	.933	.910	.949	.021	.930	.896	.950	.023	.864	.843	.883	.072	.879	.868	.906	.055
BiaNet [49]	.915	.903	.934	.039	.904	.879	.926	.043	.931	.910	.948	.021	.925	.894	.948	.024	.845	.834	.871	.085	.883	.873	.913	.052
CoNet [47]	.911	.903	.944	.036	.896	.877	.939	.040	.906	.880	.939	.026	.900	.859	.937	.030	.842	.834	.886	.077	.868	.855	.915	.054
UCNet [3]	.897	.886	.930	.043	.903	.884	.938	.039	.934	.919	.967	.019	.920	.891	.951	.025	.864	.855	.901	.066	.875	.867	.914	.051
JLDCF [35]	.902	.885	.935	.041	.903	.873	.936	.040	.931	.907	.959	.021	.925	.894	.955	.022	.862	.848	.894	.070	.880	.873	.918	.049
VST [70]	.922	.898	.939	.035	.913	.879	.937	.038	.943	.920	.965	.017	.932	.897	.951	.024	.882	.871	.917	.061	.904	.894	.933	.040
GTSOD [71]	.929	.924	.956	.028	.916	.898	.950	.032	.945	.928	.971	.016	.938	.921	.966	.018	.872	.862	.901	.066	.906	.908	.940	.037

TABLE 11
Performance comparison with benchmark weakly-supervised RGB SOD models.

Method	DUTS [6]				ECSSD [109]				DUT [11]				HKU-IS [17]				PASCAL-S [110]				SOD [111]			
	$S_\alpha \uparrow$	$F_\beta \uparrow$	$E_\xi \uparrow$	$\mathcal{M} \downarrow$	$S_\alpha \uparrow$	$F_\beta \uparrow$	$E_\xi \uparrow$	$\mathcal{M} \downarrow$	$S_\alpha \uparrow$	$F_\beta \uparrow$	$E_\xi \uparrow$	$\mathcal{M} \downarrow$	$S_\alpha \uparrow$	$F_\beta \uparrow$	$E_\xi \uparrow$	$\mathcal{M} \downarrow$	$S_\alpha \uparrow$	$F_\beta \uparrow$	$E_\xi \uparrow$	$\mathcal{M} \downarrow$	$S_\alpha \uparrow$	$F_\beta \uparrow$	$E_\xi \uparrow$	$\mathcal{M} \downarrow$
CIGAN	.834	.779	.887	.056	.896	.890	.938	.044	.799	.713	.838	.070	.886	.873	.938	.039	.827	.810	.880	.079	.800	.793	.855	.083
TIGAN	.855	.814	.918	.043	.905	.905	.950	.037	.826	.760	.874	.058	.893	.887	.949	.035	.844	.839	.902	.066	.811	.810	.872	.082
SSAL [5]	.803	.747	.865	.062	.863	.865	.908	.061	.785	.702	.835	.068	.865	.858	.923	.047	.798	.773	.854	.093	.750	.743	.801	.108
WSS [6]	.748	.633	.806	.100	.808	.774	.801	.106	.730	.590	.729	.110	.822	.773	.819	.079	.701	.691	.687	.187	.698	.635	.687	.152
C2S [128]	.805	.718	.845	.071	-	-	-	-	.773	.665	.810	.082	.869	.837	.910	.053	.784	.806	.813	.130	.770	.741	.799	.117
SCWS [96]	.841	.818	.901	.049	.879	.894	.924	.051	.813	.751	.856	.060	.883	.892	.938	.038	.821	.815	.877	.078	.782	.791	.833	.090

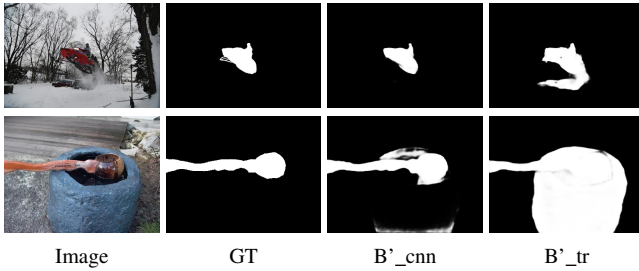


Fig. 16. Failure cases of the transformer backbone compared with the CNN backbone based framework for RGB SOD.

based model with regard to different numbers of training examples explains its effectiveness. At the same time, we observe that the model performance is not always increasing with a larger training dataset, which inspires us to work on an active learning-based transformer network to actively select representative samples for model training.

Model performance with different decoders: To test how the transformer encoder performs with different decoders, we change the backbone of existing SOD models (SCRN [1] and F3Net [2]) to transformer backbone [24], and show their performance in

Table 8, where “*” is the transformer backbone based counterpart. Table 8 shows that the transformer backbone can indeed improve the performance of existing SOD models. However, we observe similar performance of model with our decoder (B'_tr) (around 1M parameters) compared with other complicated decoders (more than 20M for both SCRN [1] and F3Net [2]). The Swin backbone model [24] has around 85M parameters, and its high capacity poses challenges to the decoder designing. We argue that the transformer-compatible decoder should be investigated to further explore the contribution of transformer encoder.

Failure Case Analysis: We further analyse when our transformer backbone based model fails, and show some samples in Fig. 16, which compares the prediction of the CNN backbone (B'_cnn) and transformer backbone (B'_tr) for RGB SOD. We observe the main less accurate predictions are those with too many false positives, which can be explained as the “double-edged sword” of the transformer backbone. On the one hand, the larger receptive field of transformer makes it superior in localizing the larger salient foreground. On the other hand, due to its larger receptive field, less salient objects that expand for a larger region can be falsely detected as positive foreground. We argue that salient object ranking [129] can be beneficial in identifying the less salient regions. We will work on it in the future.

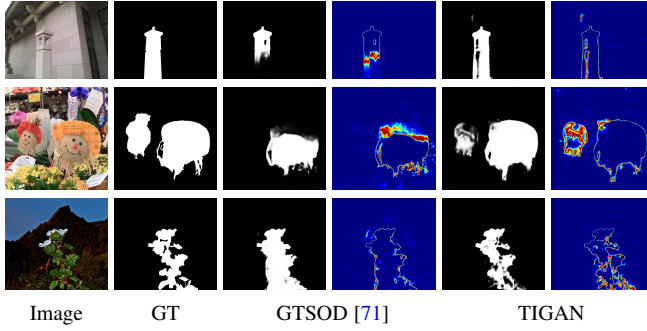


Fig. 17. Performance comparison with existing generative SOD model GTSOD [71], where prediction in each block is the model prediction and the corresponding uncertainty map.

9 PERFORMANCE COMPARISON WITH BENCHMARK SOD MODELS

In Section 6 and 7, we analysed the proposed accurate and reliable transformer based framework for both fully and weakly supervised SOD. We then comprehensively discussed the transformer backbone based saliency models in Section 8. In this Section, we compare the proposed framework with benchmark saliency models and show model performance in Tables 9, 10 and 11. Note that, VST [70] and GTSOD [71] are two existing transformer based saliency detection models.

Comparing our CNN based generative model (CIGAN) with existing techniques in Tables 9 and 10, we observe competitive performance. Note that, to focus on explaining the superior performance of transformer backbone for SOD, our decoder is simple, with only 1M parameters, which is around 5% of model parameters of existing techniques. Further, we find better performance of our generative model (TIGAN) compared with VST [70], indicating the superiority of the proposed model. Different from the deterministic VST [70], as a generative model, we aim to produce stochastic predictions leading to reliable saliency prediction. In this way, we compare with GTSOD [71], another generative transformer SOD model, in the way of both accurate and reliable saliency prediction. Tables 9 and 10 show that the proposed iGAN achieves comparable performance compared with GTSOD [71], leading to an alternative generative saliency transformer. In Fig. 17, we further visualize the produced uncertainty maps of GTSOD [71] and ours for RGB SOD. The more reliable uncertainty maps, highlighting the less confident or hard regions, further explain our superiority.

10 DISCUSSION AND CONCLUSION

In this paper, we study the generative transformer for accurate and reliable SOD. Specifically, we propose an inferential GAN within the transformer framework for both fully and weakly supervised SOD. Different from typical GANs that define the prior distribution as standard normal distribution, we infer the latent variable via Langevin Dynamics [27], a gradient based MCMC, leading to image-conditioned prior distribution. With extensive experiments, we observe that larger receptive field of the transformer leads to its better performance on image with larger salient objects (see Fig. 9). However, we also find the double-edged sword effect of the larger receptive field that leads to serious false positive (see Fig. 16). Further, for RGB-D SOD, we find that the various depth

contrast distributions lead to different depth contribution for RGB-D SOD. We then present auxiliary depth estimation, leading to consistent depth contribution (see Table 2). For weakly supervised SOD, we observe that the accurate structure information encoded in the transformer backbone as shown in Fig. 11 makes it powerful in generating structure-preserving predictions (see Table 5). Extensive experimental results demonstrate the superiority of our transformer backbone-based generative network, achieving new benchmarks with reliable uncertainty maps.

The proposed new generative model (iGAN) aims to estimate the reliability of saliency prediction with uncertainty maps. As there exists no proper evaluation metrics for uncertainty map quality estimation, we mainly visualize the uncertainty maps of each generative model. Our future work includes two main parts. Firstly, we will apply the produced uncertainty map (see Fig. 8 and Fig. 13) to the saliency generator for effective hard-negative mining. In this way, the uncertainty map can not only explain model predictions, but also serves as important prior for effective model learning. Secondly, uncertainty map quality estimation methods are needed to quantitatively analyse the quality of uncertainty maps.

REFERENCES

- [1] Z. Wu, L. Su, and Q. Huang, “Stacked cross refinement network for edge-aware salient object detection,” in *IEEE International Conference on Computer Vision (ICCV)*, pp. 7264–7273, 2019.
- [2] J. Wei, S. Wang, and Q. Huang, “F³net: Fusion, feedback and focus for salient object detection,” in *AAAI Conference on Artificial Intelligence (AAAI)*, pp. 12321–12328, 2020.
- [3] J. Zhang, D.-P. Fan, Y. Dai, S. Anwar, F. S. Saleh, T. Zhang, and N. Barnes, “UC-Net: Uncertainty inspired RGB-D saliency detection via conditional variational autoencoders,” in *IEEE Conference on Computer Vision and Pattern Recognition (CVPR)*, pp. 8582–8591, 2020.
- [4] D.-P. Fan, Y. Zhai, A. Borji, J. Yang, and L. Shao, “BBS-Net: RGB-D salient object detection with a bifurcated backbone strategy network,” in *European Conference on Computer Vision (ECCV)*, pp. 275–292, 2020.
- [5] J. Zhang, X. Yu, A. Li, P. Song, B. Liu, and Y. Dai, “Weakly-supervised salient object detection via scribble annotations,” in *IEEE Conference on Computer Vision and Pattern Recognition (CVPR)*, pp. 12546–12555, 2020.
- [6] L. Wang, H. Lu, Y. Wang, M. Feng, D. Wang, B. Yin, and X. Ruan, “Learning to detect salient objects with image-level supervision,” in *IEEE Conference on Computer Vision and Pattern Recognition (CVPR)*, pp. 136–145, 2017.
- [7] W. Wang, Q. Lai, H. Fu, J. Shen, H. Ling, and R. Yang, “Salient object detection in the deep learning era: An in-depth survey,” *IEEE Transactions on Pattern Analysis and Machine Intelligence (TPAMI)*, 2021.
- [8] J. Zhang, T. Zhang, Y. Dai, M. Harandi, and R. Hartley, “Deep unsupervised saliency detection: A multiple noisy labeling perspective,” in *IEEE Conference on Computer Vision and Pattern Recognition (CVPR)*, pp. 9029–9038, 2018.
- [9] D. T. Nguyen, M. Dax, C. K. Mummadi, T. P. N. Ngo, T. H. P. Nguyen, Z. Lou, and T. Brox, “DeepUSPS: Deep robust unsupervised saliency prediction with self-supervision,” in *Conference on Neural Information Processing Systems (NeurIPS)*, 2019.
- [10] W. Zhu, S. Liang, Y. Wei, and J. Sun, “Saliency optimization from robust background detection,” in *IEEE Conference on Computer Vision and Pattern Recognition (CVPR)*, pp. 2814–2821, 2014.
- [11] C. Yang, L. Zhang, H. Lu, X. Ruan, and M.-H. Yang, “Saliency detection via graph-based manifold ranking,” in *IEEE Conference on Computer Vision and Pattern Recognition (CVPR)*, pp. 3166–3173, 2013.
- [12] M.-M. Cheng, N. J. Mitra, X. Huang, P. H. Torr, and S.-M. Hu, “Global contrast based salient region detection,” *IEEE Transactions on Pattern Analysis and Machine Intelligence (TPAMI)*, vol. 37, no. 3, pp. 569–582, 2014.
- [13] Z. Luo, A. Mishra, A. Achkar, J. Eichel, S. Li, and P.-M. Jodoin, “Non-local deep features for salient object detection,” in *IEEE Conference on Computer Vision and Pattern Recognition (CVPR)*, pp. 6609–6617, 2017.

- [14] N. Liu, J. Han, and M.-H. Yang, "Picanet: Learning pixel-wise contextual attention for saliency detection," in *IEEE Conference on Computer Vision and Pattern Recognition (CVPR)*, pp. 3089–3098, 2018.
- [15] L. Itti, C. Koch, and E. Niebur, "A model of saliency-based visual attention for rapid scene analysis," *IEEE Transactions on Pattern Analysis and Machine Intelligence (TPAMI)*, vol. 20, no. 11, pp. 1254–1259, 1998.
- [16] R. Achanta, S. Hemami, F. Estrada, and S. Susstrunk, "Frequency-tuned salient region detection," in *IEEE Conference on Computer Vision and Pattern Recognition (CVPR)*, pp. 1597–1604, 2009.
- [17] G. Li and Y. Yu, "Visual saliency based on multiscale deep features," in *IEEE Conference on Computer Vision and Pattern Recognition (CVPR)*, pp. 5455–5463, 2015.
- [18] K. Simonyan and A. Zisserman, "Very deep convolutional networks for large-scale image recognition," in *International Conference on Learning Representations (ICLR)*, 2015.
- [19] K. He, X. Zhang, S. Ren, and J. Sun, "Deep residual learning for image recognition," in *IEEE Conference on Computer Vision and Pattern Recognition (CVPR)*, pp. 770–778, 2016.
- [20] Z. Wu, L. Su, and Q. Huang, "Cascaded partial decoder for fast and accurate salient object detection," in *IEEE Conference on Computer Vision and Pattern Recognition (CVPR)*, pp. 3907–3916, 2019.
- [21] W. Luo, Y. Li, R. Urtasun, and R. Zemel, "Understanding the effective receptive field in deep convolutional neural networks," in *Conference on Neural Information Processing Systems (NeurIPS)*, pp. 4905–4913, 2016.
- [22] A. Vaswani, N. Shazeer, N. Parmar, J. Uszkoreit, L. Jones, A. N. Gomez, L. Kaiser, and I. Polosukhin, "Attention is all you need," in *Conference on Neural Information Processing Systems (NeurIPS)*, pp. 5998–6008, 2017.
- [23] R. Ranftl, A. Bochkovskiy, and V. Koltun, "Vision transformers for dense prediction," in *IEEE International Conference on Computer Vision (ICCV)*, pp. 12179–12188, 2021.
- [24] Z. Liu, Y. Lin, Y. Cao, H. Hu, Y. Wei, Z. Zhang, S. Lin, and B. Guo, "Swin transformer: Hierarchical vision transformer using shifted windows," in *IEEE International Conference on Computer Vision (ICCV)*, pp. 10012–10022, 2021.
- [25] C. Guo, G. Pleiss, Y. Sun, and K. Q. Weinberger, "On calibration of modern neural networks," in *International Conference on Machine Learning (ICML)*, pp. 1321–1330, 2017.
- [26] I. Goodfellow, J. Pouget-Abadie, M. Mirza, B. Xu, D. Warde-Farley, S. Ozair, A. Courville, and Y. Bengio, "Generative adversarial nets," in *Conference on Neural Information Processing Systems (NeurIPS)*, vol. 27, pp. 2672–2680, 2014.
- [27] R. Neal, "Mcmc using hamiltonian dynamics," *Handbook of Markov Chain Monte Carlo*, 2011.
- [28] A. Kendall and Y. Gal, "What uncertainties do we need in bayesian deep learning for computer vision?," in *Conference on Neural Information Processing Systems (NeurIPS)*, vol. 30, 2017.
- [29] A. Dosovitskiy, L. Beyer, A. Kolesnikov, D. Weissenborn, X. Zhai, T. Unterthiner, M. Dehghani, M. Minderer, G. Heigold, S. Gelly, J. Uszkoreit, and N. Houlsby, "An image is worth 16x16 words: Transformers for image recognition at scale," in *International Conference on Learning Representations (ICLR)*, 2021.
- [30] B. Wang, Q. Chen, M. Zhou, Z. Zhang, X. Jin, and K. Gai, "Progressive feature polishing network for salient object detection," in *AAAI Conference on Artificial Intelligence (AAAI)*, pp. 12128–12135, 2020.
- [31] X. Qin, Z. Zhang, C. Huang, C. Gao, M. Dehghan, and M. Jagersand, "Basnet: Boundary-aware salient object detection," in *IEEE Conference on Computer Vision and Pattern Recognition (CVPR)*, pp. 7479–7489, 2019.
- [32] Y. Pang, X. Zhao, L. Zhang, and H. Lu, "Multi-scale interactive network for salient object detection," in *IEEE Conference on Computer Vision and Pattern Recognition (CVPR)*, pp. 9413–9422, 2020.
- [33] L. Tang, B. Li, Y. Zhong, S. Ding, and M. Song, "Disentangled high quality salient object detection," in *IEEE International Conference on Computer Vision (ICCV)*, pp. 3580–3590, 2021.
- [34] M. Zhang, T. Liu, Y. Piao, S. Yao, and H. Lu, "Auto-msfnet: Search multi-scale fusion network for salient object detection," in *ACM International Conference on Multimedia (MM)*, pp. 667–676, 2021.
- [35] K. Fu, D.-P. Fan, G.-P. Ji, and Q. Zhao, "JL-DCF: Joint learning and densely-cooperative fusion framework for RGB-D salient object detection," in *IEEE Conference on Computer Vision and Pattern Recognition (CVPR)*, pp. 3052–3062, 2020.
- [36] Y. Piao, W. Ji, J. Li, M. Zhang, and H. Lu, "Depth-induced multi-scale recurrent attention network for saliency detection," in *IEEE International Conference on Computer Vision (ICCV)*, pp. 7254–7263, 2019.
- [37] L. Qu, S. He, J. Zhang, J. Tian, Y. Tang, and Q. Yang, "RGBD salient object detection via deep fusion," *IEEE Transactions on Image Processing (TIP)*, vol. 26, no. 5, pp. 2274–2285, 2017.
- [38] N. Wang and X. Gong, "Adaptive fusion for RGB-D salient object detection," *IEEE Access*, vol. 7, pp. 55277–55284, 2019.
- [39] J. Han, H. Chen, N. Liu, C. Yan, and X. Li, "CNNs-based RGB-D saliency detection via cross-view transfer and multiview fusion," *IEEE Transactions on Cybernetics*, vol. 48, no. 11, pp. 3171–3183, 2017.
- [40] Y. Piao, Z. Rong, M. Zhang, W. Ren, and H. Lu, "A2dele: Adaptive and attentive depth distiller for efficient RGB-D salient object detection," in *IEEE Conference on Computer Vision and Pattern Recognition (CVPR)*, pp. 9060–9069, 2020.
- [41] H. Chen and Y. Li, "Progressively complementarity-aware fusion network for RGB-D salient object detection," in *IEEE Conference on Computer Vision and Pattern Recognition (CVPR)*, pp. 3051–3060, 2018.
- [42] H. Chen, Y. Li, and D. Su, "Multi-modal fusion network with multi-scale multi-path and cross-modal interactions for RGB-D salient object detection," *Pattern Recognition (PR)*, vol. 86, pp. 376–385, 2019.
- [43] H. Chen and Y. Li, "Three-stream attention-aware network for RGB-D salient object detection," *IEEE Transactions on Image Processing (TIP)*, vol. 28, no. 6, pp. 2825–2835, 2019.
- [44] J.-X. Zhao, Y. Cao, D.-P. Fan, M.-M. Cheng, X.-Y. Li, and L. Zhang, "Contrast prior and fluid pyramid integration for RGBD salient object detection," in *IEEE Conference on Computer Vision and Pattern Recognition (CVPR)*, pp. 3927–3936, 2019.
- [45] M. Zhang, W. Ren, Y. Piao, Z. Rong, and H. Lu, "Select, supplement and focus for RGB-D saliency detection," in *IEEE Conference on Computer Vision and Pattern Recognition (CVPR)*, pp. 3472–3481, 2020.
- [46] N. Liu, N. Zhang, and J. Han, "Learning selective self-mutual attention for RGB-D saliency detection," in *IEEE Conference on Computer Vision and Pattern Recognition (CVPR)*, pp. 13756–13765, 2020.
- [47] W. Ji, J. Li, M. Zhang, Y. Piao, and H. Lu, "Accurate RGB-D salient object detection via collaborative learning," in *European Conference on Computer Vision (ECCV)*, pp. 52–69, 2020.
- [48] Y. Pang, L. Zhang, X. Zhao, and H. Lu, "Hierarchical dynamic filtering network for RGB-D salient object detection," in *European Conference on Computer Vision (ECCV)*, pp. 235–252, 2020.
- [49] Z. Zhang, Z. Lin, J. Xu, W.-D. Jin, S.-P. Lu, and D.-P. Fan, "Bilateral attention network for RGB-D salient object detection," *IEEE Transactions on Image Processing (TIP)*, vol. 30, pp. 1949–1961, 2021.
- [50] C. Li, R. Cong, Y. Piao, Q. Xu, and C. C. Loy, "RGB-D salient object detection with cross-modality modulation and selection," in *European Conference on Computer Vision (ECCV)*, pp. 225–241, 2020.
- [51] G. Li, Z. Liu, L. Ye, Y. Wang, and H. Ling, "Cross-modal weighting network for RGB-D salient object detection," in *European Conference on Computer Vision (ECCV)*, pp. 665–681, 2020.
- [52] J. Zhang, D.-P. Fan, Y. Dai, X. Yu, Y. Zhong, N. Barnes, and L. Shao, "Rgb-d saliency detection via cascaded mutual information minimization," in *IEEE International Conference on Computer Vision (ICCV)*, pp. 4338–4347, 2021.
- [53] A. Luo, X. Li, F. Yang, Z. Jiao, H. Cheng, and S. Lyu, "Cascade graph neural networks for RGB-D salient object detection," in *European Conference on Computer Vision (ECCV)*, pp. 346–364, 2020.
- [54] S. Chen and Y. Fu, "Progressively guided alternate refinement network for RGB-D salient object detection," in *European Conference on Computer Vision (ECCV)*, pp. 520–538, 2020.
- [55] M. Zhang, S. X. Fei, J. Liu, S. Xu, Y. Piao, and H. Lu, "Asymmetric two-stream architecture for accurate RGB-D saliency detection," in *European Conference on Computer Vision (ECCV)*, pp. 374–390, 2020.
- [56] G. Li, Z. Liu, M. Chen, Z. Bai, W. Lin, and H. Ling, "Hierarchical alternate interaction network for rgb-d salient object detection," *IEEE Transactions on Image Processing (TIP)*, vol. 30, pp. 3528–3542, 2021.
- [57] K. Fu, D.-P. Fan, G.-P. Ji, Q. Zhao, J. Shen, and C. Zhu, "Siamese network for rgb-d salient object detection and beyond," *IEEE Transactions on Pattern Analysis and Machine Intelligence (TPAMI)*, 2021.
- [58] N. Carion, F. Massa, G. Synnaeve, N. Usunier, A. Kirillov, and S. Zagoruyko, "End-to-end object detection with transformers," in *European Conference on Computer Vision (ECCV)*, pp. 213–229, 2020.
- [59] X. Zhu, W. Su, L. Lu, B. Li, X. Wang, and J. Dai, "Deformable DETR: Deformable transformers for end-to-end object detection," in *International Conference on Learning Representations (ICLR)*, 2021.
- [60] Z. Dai, B. Cai, Y. Lin, and J. Chen, "UP-DETR: Unsupervised pre-training for object detection with transformers," in *IEEE Conference*

- on *Computer Vision and Pattern Recognition (CVPR)*, pp. 1601–1610, 2021.
- [61] W. Wang, E. Xie, X. Li, D.-P. Fan, K. Song, D. Liang, T. Lu, P. Luo, and L. Shao, “Pyramid vision transformer: A versatile backbone for dense prediction without convolutions,” in *IEEE International Conference on Computer Vision (ICCV)*, pp. 568–578, 2021.
- [62] G. Zhang, Z. Luo, K. Cui, and S. Lu, “Meta-DETR: Few-shot object detection via unified image-level meta-learning,” *arXiv preprint arXiv:2103.11731*, 2021.
- [63] Y. Xu, Y. Ban, G. Delorme, C. Gan, D. Rus, and X. Alameddine, “TransCenter: Transformers with dense queries for multiple-object tracking,” *arXiv preprint arXiv:2103.15145*, 2021.
- [64] P. Chu, J. Wang, Q. You, H. Ling, and Z. Liu, “TransMOT: Spatial-temporal graph transformer for multiple object tracking,” *arXiv preprint arXiv:2104.00194*, 2021.
- [65] B. Yan, H. Peng, J. Fu, D. Wang, and H. Lu, “Learning spatio-temporal transformer for visual tracking,” in *IEEE International Conference on Computer Vision (ICCV)*, pp. 10448–10457, 2021.
- [66] W. Mao, Y. Ge, C. Shen, Z. Tian, X. Wang, and Z. Wang, “TF-Pose: Direct human pose estimation with transformers,” *arXiv preprint arXiv:2103.15320*, 2021.
- [67] L. Stof, M. Vidal, and A. Mathis, “End-to-End trainable Multi-Instance pose estimation with transformers,” *arXiv preprint arXiv:2103.12115*, 2021.
- [68] S. Jiang, D. Campbell, Y. Lu, H. Li, and R. Hartley, “Learning to estimate hidden motions with global motion aggregation,” in *IEEE International Conference on Computer Vision (ICCV)*, pp. 9772–9781, 2021.
- [69] S. Zheng, J. Lu, H. Zhao, X. Zhu, Z. Luo, Y. Wang, Y. Fu, J. Feng, T. Xiang, P. H. Torr, and L. Zhang, “Rethinking semantic segmentation from a sequence-to-sequence perspective with transformers,” in *IEEE Conference on Computer Vision and Pattern Recognition (CVPR)*, pp. 6881–6890, 2021.
- [70] N. Liu, N. Zhang, K. Wan, L. Shao, and J. Han, “Visual saliency transformer,” in *IEEE International Conference on Computer Vision (ICCV)*, pp. 4722–4732, 2021.
- [71] J. Zhang, J. Xie, N. Barnes, and P. Li, “Learning generative vision transformer with energy-based latent space for saliency prediction,” in *Conference on Neural Information Processing Systems (NeurIPS)*, vol. 34, 2021.
- [72] Y. LeCun, S. Chopra, R. Hadsell, F. J. Huang, and et al., “A tutorial on energy-based learning,” in *PREDICTING STRUCTURED DATA*, MIT Press, 2006.
- [73] D. Kingma and M. Welling, “Auto-encoding variational bayes,” in *International Conference on Learning Representations (ICLR)*, 2014.
- [74] K. Sohn, H. Lee, and X. Yan, “Learning structured output representation using deep conditional generative models,” in *Conference on Neural Information Processing Systems (NIPS)*, pp. 3483–3491, 2015.
- [75] C. F. Baumgartner, K. C. Tezcan, K. Chaitanya, A. M. Hötter, U. J. Muehlemaier, K. Schawkat, A. S. Becker, O. Donati, and E. Konukoglu, “Phiseg: Capturing uncertainty in medical image segmentation,” in *International Conference on Medical Image Computing and Computer-Assisted Intervention (MICCAI)*, pp. 119–127, 2019.
- [76] S. Kohl, B. Romera-Paredes, C. Meyer, J. De Fauw, J. R. Ledsam, K. Maier-Hein, S. M. A. Eslami, D. Jimenez Rezende, and O. Ronneberger, “A probabilistic u-net for segmentation of ambiguous images,” in *Conference on Neural Information Processing Systems (NeurIPS)*, pp. 6965–6975, 2018.
- [77] B. Li, Z. Sun, and Y. Guo, “Supervae: Superpixelwise variational autoencoder for salient object detection,” in *AAAI Conference on Artificial Intelligence (AAAI)*, pp. 8569–8576, 2019.
- [78] J. Zhang, D.-P. Fan, Y. Dai, S. Anwar, F. S. Saleh, S. Aliakbarian, and N. Barnes, “Uncertainty inspired rgb-d saliency detection,” *IEEE Transactions on Pattern Analysis and Machine Intelligence (TPAMI)*, 2021.
- [79] R. Groenendijk, S. Karaoglu, T. Gevers, and T. Mensink, “On the benefit of adversarial training for monocular depth estimation,” *Computer Vision and Image Understanding*, vol. 190, p. 102848, 2020.
- [80] Q. H. Le, K. Youcef-Toumi, D. Tsetserukou, and A. Jahanian, “Gan mask r-cnn: instance semantic segmentation benefits from generative adversarial networks,” *arXiv preprint arXiv:2010.13757*, 2020.
- [81] N. Souly, C. Spampinato, and M. Shah, “Semi supervised semantic segmentation using generative adversarial network,” in *IEEE International Conference on Computer Vision (ICCV)*, pp. 5689–5697, 2017.
- [82] W.-C. Hung, Y.-H. Tsai, Y.-T. Liou, Y.-Y. Lin, and M.-H. Yang, “Adversarial learning for semi-supervised semantic segmentation,” in *British Machine Vision Conference (BMVC)*, 2018.
- [83] Y. Chen, Q. Gao, and X. Wang, “Inferential wasserstein generative adversarial networks,” *arXiv preprint arXiv:2109.05652*, 2021.
- [84] K.-J. Hsu, Y.-Y. Lin, and Y.-Y. Chuang, “Weakly supervised saliency detection with a category-driven map generator,” *British Machine Vision Conference (BMVC)*, 2017.
- [85] G. Li, Y. Xie, and L. Lin, “Weakly supervised salient object detection using image labels,” in *AAAI Conference on Artificial Intelligence (AAAI)*, 2018.
- [86] J. Ahn and S. Kwak, “Learning pixel-level semantic affinity with image-level supervision for weakly supervised semantic segmentation,” in *IEEE Conference on Computer Vision and Pattern Recognition (CVPR)*, pp. 4981–4990, 2018.
- [87] Z. Huang, X. Wang, J. Wang, W. Liu, and J. Wang, “Weakly-supervised semantic segmentation network with deep seeded region growing,” in *IEEE Conference on Computer Vision and Pattern Recognition (CVPR)*, pp. 7014–7023, 2018.
- [88] H. Zhang, Y. Zeng, H. Lu, L. Zhang, J. Li, and J. Qi, “Learning to detect salient object with multi-source weak supervision,” *IEEE Transactions on Pattern Analysis and Machine Intelligence*, 2021.
- [89] C. Song, Y. Huang, W. Ouyang, and L. Wang, “Box-driven class-wise region masking and filling rate guided loss for weakly supervised semantic segmentation,” in *IEEE Conference on Computer Vision and Pattern Recognition (CVPR)*, pp. 3136–3145, 2019.
- [90] J. Dai, K. He, and J. Sun, “Boxsup: Exploiting bounding boxes to supervise convolutional networks for semantic segmentation,” in *IEEE International Conference on Computer Vision (ICCV)*, pp. 1635–1643, 2015.
- [91] V. Kulharia, S. Chandra, A. Agrawal, P. Torr, and A. Tyagi, “Box2seg: Attention weighted loss and discriminative feature learning for weakly supervised segmentation,” in *European Conference on Computer Vision (ECCV)*, pp. 290–308, 2020.
- [92] J. Lee, J. Yi, C. Shin, and S. Yoon, “Bbam: Bounding box attribution map for weakly supervised semantic and instance segmentation,” in *IEEE Conference on Computer Vision and Pattern Recognition (CVPR)*, pp. 2643–2652, 2021.
- [93] Z. Tian, C. Shen, X. Wang, and H. Chen, “Boxinst: High-performance instance segmentation with box annotations,” in *IEEE Conference on Computer Vision and Pattern Recognition (CVPR)*, pp. 5443–5452, 2021.
- [94] D. Lin, J. Dai, J. Jia, K. He, and J. Sun, “Scribblesup: Scribble-supervised convolutional networks for semantic segmentation,” in *IEEE Conference on Computer Vision and Pattern Recognition (CVPR)*, pp. 3159–3167, 2016.
- [95] P. Vernaza and M. Chandraker, “Learning random-walk label propagation for weakly-supervised semantic segmentation,” in *IEEE Conference on Computer Vision and Pattern Recognition (CVPR)*, pp. 7158–7166, 2017.
- [96] S. Yu, B. Zhang, J. Xiao, and E. G. Lim, “Structure-consistent weakly supervised salient object detection with local saliency coherence,” in *AAAI Conference on Artificial Intelligence (AAAI)*, pp. 3234–3242, 2021.
- [97] A. Bearman, O. Russakovsky, V. Ferrari, and L. Fei-Fei, “What’s the point: Semantic segmentation with point supervision,” in *European Conference on Computer Vision (ECCV)*, pp. 549–565, 2016.
- [98] R. A. McEver and B. Manjunath, “Pcams: Weakly supervised semantic segmentation using point supervision,” *arXiv preprint arXiv:2007.05615*, 2020.
- [99] H. Chen, J. Wang, H. C. Chen, X. Zhen, F. Zheng, R. Ji, and L. Shao, “Seminar learning for click-level weakly supervised semantic segmentation,” in *IEEE International Conference on Computer Vision (ICCV)*, pp. 6920–6929, 2021.
- [100] A. Obukhov, S. Georgoulis, D. Dai, and L. Van Gool, “Gated CRF loss for weakly supervised semantic image segmentation,” in *Conference on Neural Information Processing Systems (NeurIPS)*, 2019.
- [101] P. Arbeláez, J. Pont-Tuset, J. T. Barron, F. Marques, and J. Malik, “Multiscale combinatorial grouping,” in *IEEE Conference on Computer Vision and Pattern Recognition (CVPR)*, pp. 328–335, 2014.
- [102] C. Rother, V. Kolmogorov, and A. Blake, “grabcut” interactive foreground extraction using iterated graph cuts,” *ACM transactions on graphics (TOG)*, vol. 23, no. 3, pp. 309–314, 2004.
- [103] J. Zhang, J. Xie, and N. Barnes, “Learning noise-aware encoder-decoder from noisy labels by alternating back-propagation for saliency detection,” in *European Conference on Computer Vision (ECCV)*, pp. 349–366, Springer, 2020.
- [104] T. Han, Y. Lu, S.-C. Zhu, and Y. N. Wu, “Alternating back-propagation for generator network,” in *AAAI Conference on Artificial Intelligence (AAAI)*, 2017.

- [105] K. Han, Y. Wang, H. Chen, X. Chen, J. Guo, Z. Liu, Y. Tang, A. Xiao, C. Xu, Y. Xu, *et al.*, “A survey on visual transformer,” *arXiv preprint arXiv:2012.12556*, 2020.
- [106] J. Kim, D. Han, Y.-W. Tai, and J. Kim, “Salient region detection via high-dimensional color transform and local spatial support,” *IEEE Transactions on Image Processing (TIP)*, vol. 25, no. 1, pp. 9–23, 2015.
- [107] C. Godard, O. Mac Aodha, and G. J. Brostow, “Unsupervised monocular depth estimation with left-right consistency,” in *IEEE Conference on Computer Vision and Pattern Recognition (CVPR)*, pp. 270–279, 2017.
- [108] J. He, D. Spokoyny, G. Neubig, and T. Berg-Kirkpatrick, “Lagging inference networks and posterior collapse in variational autoencoders,” in *International Conference on Learning Representations (ICLR)*, 2019.
- [109] Q. Yan, L. Xu, J. Shi, and J. Jia, “Hierarchical saliency detection,” in *IEEE Conference on Computer Vision and Pattern Recognition (CVPR)*, pp. 1155–1162, 2013.
- [110] Y. Li, X. Hou, C. Koch, J. M. Rehg, and A. L. Yuille, “The secrets of salient object segmentation,” in *IEEE Conference on Computer Vision and Pattern Recognition (CVPR)*, pp. 280–287, 2014.
- [111] V. Movahedi and J. H. Elder, “Design and perceptual validation of performance measures for salient object segmentation,” in *IEEE Conference on Computer Vision and Pattern Recognition (CVPR) Workshop*, pp. 49–56, 2010.
- [112] R. Ju, Y. Liu, T. Ren, L. Ge, and G. Wu, “Depth-aware salient object detection using anisotropic center-surround difference,” *Signal Processing: Image Communication*, vol. 38, pp. 115–126, 2015.
- [113] Y. Niu, Y. Geng, X. Li, and F. Liu, “Leveraging stereopsis for saliency analysis,” in *IEEE Conference on Computer Vision and Pattern Recognition (CVPR)*, pp. 454–461, 2012.
- [114] Y. Cheng, H. Fu, X. Wei, J. Xiao, and X. Cao, “Depth enhanced saliency detection method,” in *Proceedings of international conference on internet multimedia computing and service*, pp. 23–27, 2014.
- [115] H. Peng, B. Li, W. Xiong, W. Hu, and R. Ji, “RGBD salient object detection: A benchmark and algorithms,” in *European Conference on Computer Vision (ECCV)*, pp. 92–109, 2014.
- [116] N. Li, J. Ye, Y. Ji, H. Ling, and J. Yu, “Saliency detection on light field,” in *IEEE Conference on Computer Vision and Pattern Recognition (CVPR)*, pp. 2806–2813, 2014.
- [117] D.-P. Fan, Z. Lin, Z. Zhang, M. Zhu, and M.-M. Cheng, “Rethinking RGB-D Salient Object Detection: Models, Datasets, and Large-Scale Benchmarks,” *IEEE Transactions on Neural Networks and Learning Systems (TNNLS)*, vol. 32, no. 5, pp. 2075–2089, 2020.
- [118] D.-P. Fan, C. Gong, Y. Cao, B. Ren, M.-M. Cheng, and A. Borji, “Enhanced-alignment measure for binary foreground map evaluation,” *International Joint Conference on Artificial Intelligence (IJCAI)*, pp. 698–704, 2018.
- [119] D.-P. Fan, M.-M. Cheng, Y. Liu, T. Li, and A. Borji, “Structure-measure: A new way to evaluate foreground maps,” in *IEEE International Conference on Computer Vision (ICCV)*, pp. 4548–4557, 2017.
- [120] J. Zhang, D.-P. Fan, Y. Dai, S. Anwar, F. Saleh, S. Aliakbarian, and N. Barnes, “Uncertainty inspired rgb-d saliency detection,” *IEEE Transactions on Pattern Analysis and Machine Intelligence (TPAMI)*, 2021.
- [121] S. Depeweg, J.-M. Hernandez-Lobato, F. Doshi-Velez, and S. Udluft, “Decomposition of uncertainty in Bayesian deep learning for efficient and risk-sensitive learning,” in *International Conference on Machine Learning (ICML)*, pp. 1184–1193, 2018.
- [122] Y. Wang, Y. Yang, Z. Yang, L. Zhao, P. Wang, and W. Xu, “Occlusion aware unsupervised learning of optical flow,” in *IEEE Conference on Computer Vision and Pattern Recognition (CVPR)*, pp. 4884–4893, 2018.
- [123] M. Naseer, K. Ranasinghe, S. Khan, M. Hayat, F. S. Khan, and M.-H. Yang, “Intriguing properties of vision transformers,” in *Conference on Neural Information Processing Systems (NeurIPS)*, 2021.
- [124] J. Deng, W. Dong, R. Socher, L.-J. Li, K. Li, and L. Fei-Fei, “Imagenet: A large-scale hierarchical image database,” in *IEEE Conference on Computer Vision and Pattern Recognition (CVPR)*, pp. 248–255, 2009.
- [125] H. Zhou, X. Xie, J.-H. Lai, Z. Chen, and L. Yang, “Interactive two-stream decoder for accurate and fast saliency detection,” in *IEEE Conference on Computer Vision and Pattern Recognition (CVPR)*, pp. 9141–9150, 2020.
- [126] B. Xu, H. Liang, R. Liang, and P. Chen, “Locate globally, segment locally: A progressive architecture with knowledge review network for salient object detection,” in *AAAI Conference on Artificial Intelligence (AAAI)*, pp. 3004–3012, 2021.
- [127] Z. Zhao, C. Xia, C. Xie, and J. Li, “Complementary trilateral decoder for fast and accurate salient object detection,” in *ACM International Conference on Multimedia (MM)*, pp. 4967–4975, 2021.
- [128] X. Li, F. Yang, H. Cheng, W. Liu, and D. Shen, “Contour knowledge transfer for salient object detection,” in *European Conference on Computer Vision (ECCV)*, pp. 355–370, 2018.
- [129] M. A. Islam, M. Kalash, and N. D. Bruce, “Revisiting salient object detection: Simultaneous detection, ranking, and subitizing of multiple salient objects,” in *IEEE Conference on Computer Vision and Pattern Recognition (CVPR)*, pp. 7142–7150, 2018.